Contact lines over random topographical substrates. Part 2. Dynamics

By By **NIKOS SAVVA**[1], **GRIGORIOS A. PAVLIOTIS**[2] AND **SERAFIM KALLIADASIS**[1]

[1]Department of Chemical Engineering, Imperial College London, London SW7 2AZ, UK

[2]Department of Mathematics, Imperial College London, London SW7 2AZ, UK

(Received 23 March 2010)

We examine the dynamics of a two-dimensional droplet spreading over a random topographical substrate. Our analysis is based on the stochastic formalism developed in Part 1 where a random substrate was modelled as band-limited white noise. The system of integrodifferential equations derived for the motion of the contact points over deterministic substrates (Savva & Kalliadasis 2009) is applicable to the case of random substrates as well. This system is linearized for small substrate amplitudes to obtain stochastic differential equations for the droplet shift and contact line fluctuations in the limit of shallow and slowly varying topographies. Our theoretical predictions for the time evolution of the statistical properties of these quantities are verified by numerical experiments. Considering the statistics of the dynamics allows us to fully address the influence of the substrate variations on wetting. For example, we demonstrate that the droplet wets the substrate less as the substrate roughness increases illustrating also the possibility of a substrate-induced hysteresis effect. Finally, the analysis of the long-time limit of spreading dynamics for a substrate represented by a band-limited white noise is extended to arbitrary substrate representations. It is shown that the statistics of spreading is independent of the characteristic lengthscales that naturally arise from the statistical properties of a substrate representation.

1. Introduction

It is a fundamental problem to understand how deterministic/random heterogeneities influence the characteristics of contact line propagation, e.g. speed and location. Theoretical studies on droplet spreading, a simple prototype for the study of contact line motion, have primarily focused on ideally flat substrates (e.g. Hocking 1983) often in the presence of other effects such as chemical heterogeneities, evaporation and thermocapillarity (e.g. Schwartz 1998; Sodtke *et al.* 2008; Rednikov *et al.* 2009; Ehrhard & Davis 1991).

The effects of substrate topography on droplet spreading dynamics, albeit known from experiments with highly-irregular micro-scale features to be significant (Cazabat & Cohen-Stuart 1986), have received far less attention. The few theoretical studies have focused on deterministic substrates. For example, Gramlich *et al.* (2004) examined the motion of a two-dimensional contact line over a topographical feature (trench or mound) by solving numerically the full Stokes equations and employing numerical slip at the contact line. Gaskell *et al.* (2004) examined droplet spreading over three-dimensional topography (wedges or trenches) by solving numerically the long-wave approximation with the computationally advantageous constant-thickness precursor film model, often used in spreading studies (see e.g. Troian *et al.* 1989; Schwartz & Eley 1998; Kalliadasis 2000). Recently, Savva & Kalliadasis (2009) examined theoretically two-dimensional droplet (referred to hereafter simply as “droplet”) spreading on spatially varying deterministic topographical substrates. They utilized the long-wave approximation with a slip model and through a singular perturbation method they obtained a system of integrodifferential equations (IDEs) for the evolution of the two moving fronts. The restriction to two dimensions implies that there are no transverse variations, essentially treating the contact lines as a set of two points.

As far as the influence of random substrates on spreading dynamics is concerned, the few previous studies on the subject are mostly based on ad hoc modeling ideas and postulated equations (Moulinet *et al.* 2002; Tanguy & Vettorel 2004; Nikolayev 2005; Katzav *et al.* 2007). To date, no attempt has been made to quantify the statistics of the dynamics on random substrates through a systematic fluid mechanics treatment based on rational approaches. Considering the statistics of the dynamics also allows us to fully assess the influence of random spatial heterogeneities on wetting.

Our starting point is the set of IDEs developed by Savva & Kalliadasis (2009). Following the formalism of Part 1, the topographical substrate is taken to be band-limited white noise. We also assume that characteristic variations of the substrate are much larger than the slip length. The governing equations are given in §2 while in §3 they are linearized for small values of the substrate amplitude to obtain a set of evolution equations for the contact line fluctuations and droplet shift. In §4 we examine the dynamics of the droplet shift and we deduce its behavior analytically through early- and long-time asymptotics. In §5 we assess the effects of substrate roughness on wetting, by considering the statistics of the contact line fluctuation. In §6 we examine effects such as droplet equilibria on "very" rough substrates and a substrate-induced hysteresis effect, demonstrating also the possibility of a stick-slip behavior that is commonly reported in experiments. Finally, in §7 we generalize the long-time limit of spreading on a substrate represented as band-limited white noise to arbitrary substrate representations. A discussion and summary of our results is offered in §8.

2. Problem formulation

We follow Part 1 and represent the substrate as a stationary random function given by a trigonometric series and defined in terms of a characteristic amplitude and wavenumber. Its form is re-written here for the reader's convenience,

$$\eta\left(x\right)=\frac{\eta_0}{\sqrt{N}}\sum_{m=1}^{N}\left[\alpha_m\sin\frac{k_0mx}{N}+\beta_m\cos\frac{k_0mx}{N}\right], \tag{2.1}$$

where η_0 and k_0 are the characteristic amplitude and wavenumber of the substrate, respectively, and N is a large positive integer. Again, α_m and β_m are statistically independent, normal random variables with $\left\langle\alpha_m^2\right\rangle=\left\langle\beta_m^2\right\rangle=1$. We note that not only is the noise term $\eta\left(x\right)$ spatial, but it enters (2.5) in a highly nonlinear fashion thus precluding the use of the standard Langevin/Fokker-Planck formalism often employed to study randomly perturbed dynamical systems (e.g. Gardiner 1985).

Our starting point is the recent study by Savva & Kalliadasis (2009) on droplet spreading over deterministic topographical substrates. For the sake of clarity and completeness we briefly review this study. These authors utilized a slip model and a long-wave expansion in the Stokes-flow regime, i.e. assumed slow flows, small contact angles and strong surface tension effects, obtaining a single equation for the evolution of the droplet thickness $H(x,t)$ over a smooth substrate $\eta(x)$. The spatial coordinate, x, and time, t, are made dimensionless by the characteristic lengthscale $L=\sqrt{A/(2\alpha_s)}$ and time $\tau=3\mu L/(\gamma\alpha_s^3)$, respectively, where A is the droplet cross-sectional area, α_s is the equilibrium contact angle, and μ, γ are is the fluid viscosity and surface tension, respectively. $H(x,t)$ and $\eta(x)$ are scaled by $L\alpha_s$. The dimensionless form of the free-surface evolution equation is

$$H_t+\partial_x\left[H^2\left(H+\lambda\right)\partial_x^3\left(H+\eta\right)\right]=0, \tag{2.2}$$

where $\lambda\ll 1$ is the non-dimensional slip length, scaled by $L\alpha_s/3$, that originates from the Navier model imposed to make integrable the stress singularity that occurs at the moving contact line (Huh & Scriven 1971). Uunlike the computationally advantageous precursor film model mentioned in §1), here we maintain a sharp contact line.

Let $a(t)$ and $b(t)$ be the right and left contact points, respectively. Equation (2.2) must be solved subject to the volume constraint

$$\int_b^a H\left(x,t\right)\,\mathrm{d}x = 2 \tag{2.3}$$

and the boundary conditions at the two contact points that the droplet thickness vanishes and the angle the free-surface makes with the substrate remains equal to its static value, α_s, so that

$$\partial_x H\big|_{x=a} = -\theta_a \quad \text{and} \quad \partial_x H\big|_{x=b} = +\theta_b, \tag{2.4a,b}$$

with

$$\theta_a = \frac{1+\alpha_s^2\eta_a'^2}{1+\alpha_s^2\eta_a'} \quad \text{and} \quad \theta_b = \frac{1+\alpha_s^2\eta_b'^2}{1-\alpha_s^2\eta_b'},$$

where we use $\partial_x\eta\big|_{x=c} = \eta_c'$. For quasi-static spreading, asymptotic matching for $\lambda \ll 1$ of the solution in the bulk of the fluid with the solutions in the vicinity of the contact lines yields the following IDEs for the time-evolution of the two moving fronts,

$$\dot{a} = +\frac{\delta_a M_b + \delta_b\phi_a M_0}{M_a M_b - \phi_a\phi_b M_0^2} \quad \text{and} \quad \dot{b} = -\frac{\delta_b M_a + \delta_a\phi_b M_0}{M_a M_b - \phi_a\phi_b M_0^2}, \tag{2.5a,b}$$

where the dots denote time-differentiation. Here we identify

$$\delta_a = \frac{1}{3}\left(\phi_a^3 - \theta_a^3\right), \tag{2.6a}$$

$$\delta_b = \frac{1}{3}\left(\phi_b^3 - \theta_b^3\right), \tag{2.6b}$$

$$M_a = \ln\left(\theta_a\frac{a-b}{\lambda}\right) + \int_{-1}^{+1}\frac{1}{1-y}\left[\frac{\phi_a^3\left(a-b\right)^3\left(1-y^2\right)^4}{128H_0^3\left(1-y\right)} - 1\right]\mathrm{d}y, \tag{2.6c}$$

$$M_b = \ln\left(\theta_b\frac{a-b}{\lambda}\right) + \int_{-1}^{+1}\frac{1}{1+y}\left[\frac{\phi_b^3\left(a-b\right)^3\left(1-y^2\right)^4}{128H_0^3\left(1+y\right)} - 1\right]\mathrm{d}y, \tag{2.6d}$$

$$M_0 = \frac{\phi_a\phi_b\left(a-b\right)^3}{128}\int_{-1}^{+1}\frac{\left(1-y^2\right)^3}{H_0^3}\,\mathrm{d}y, \tag{2.6e}$$

where

$$\begin{aligned}\phi_a &= \frac{2}{a-b}\left[\frac{6}{a-b}+3\bar{\eta}-2\eta_a-\eta_b+\frac{1}{2}\eta'_a\left(a-b\right)\right],\\ \phi_b &= \frac{2}{a-b}\left[\frac{6}{a-b}+3\bar{\eta}-2\eta_b-\eta_a-\frac{1}{2}\eta'_b\left(a-b\right)\right],\end{aligned}$$

correspond to the "mesoscopic" contact angles at $x = a$ and b, respectively, observed at distances where the substrate features are sufficiently resolved (a schematic illustrating the different contact lines is given in the study by Savva & Kalliadasis (2009)) and y, a coordinate introduced to facilitate the analysis, is defined from $x = (a-b)y/2+(a+b)/2$ (so that the domain $a \leqslant x \leqslant b$ is mapped to $-1 \leqslant y \leqslant +1$). Also,

$$H_0\left(y\right) = \frac{3}{2}\left[\frac{2}{a-b}+\bar{\eta}-\frac{1}{2}\left(\eta_a+\eta_b\right)\right]\left(1-y^2\right)+\frac{1}{2}\left[\eta_a\left(1+y\right)+\eta_b\left(1-y\right)\right]-\eta\left(x\right),$$

is the leading-order solution in the bulk of the droplet with $\eta_a = \eta\left(a\right)$, $\eta_b = \eta\left(b\right)$ and $\bar{\eta} = \int_b^a \eta\left(\xi\right)\,\mathrm{d}\xi/\left(a-b\right)$. Savva & Kalliadasis (2009) confirmed the validity of (2.5) through detailed comparisons with numerical solutions to the full equation, (2.2). In addition, they examined many qualitative features of droplet spreading, but they restricted their attention to deterministic substrates only.

3. Derivation of leading-order equations for droplet shift and contact line fluctuations

Analytical progress can be made by assuming a small substrate amplitude which then allows us to linearize (2.5) around the flat-substrate case. Proceeding as in Part 1, we introduce the droplet shift, ℓ, and contact line fluctuation, ε, that allows us to split the droplet motion into two separate components. The former accounts for a sliding motion along the topographical features whereas the latter accounts for deviations from the droplet radius of the flat-substrate spreading dynamics. This distinction results into the following dynamical system,

$$\dot{\varepsilon} = \frac{1}{2}\left(\dot{a} - \dot{b}\right) - \dot{x}_0, \quad \dot{\ell} = \frac{1}{2}\left(\dot{a} + \dot{b}\right), \tag{3.1a, b}$$

where $x_0(t)$ is the the flat-substrate droplet radius given by the solution to the differential equation

$$3\dot{x}_0 \ln \frac{2x_0}{\lambda e^2} = \frac{27}{x_0^6} - 1, \tag{3.2}$$

which approaches $\sqrt{3}$ in the long-time limit. In order to express the right-hand sides of (3.1) in terms of ℓ and ε we employ a linearization procedure which treats ε as $O\left(\eta_0\right)$, retaining only the linear terms in η_0 and ε. As with the statics, the linearization is valid provided that:

$$\eta_0 k_0^2 \ll 1. \tag{3.3}$$

The derivation of the linearized equations is rather lengthy and tedious, but through certain algebraic manipulations more compact and manageable expressions can be obtained at the end. Most notably, we negate the integration variable for the integral in (2.6d), whereas for (2.6e) we take

$$M_0 = \frac{\phi_a \phi_b \left(a - b\right)^3}{256} \int_{-1}^{+1} \left(1 - y^2\right)^3 \left\{ \frac{1}{\left[H_0\left(-y\right)\right]^3} + \frac{1}{\left[H_0\left(+y\right)\right]^3} \right\} \mathrm{d}y, \tag{3.4}$$

which becomes

$$\begin{aligned} M_0 = \frac{x_0^2}{3} \Bigg\{ & 1 + 2\frac{\varepsilon}{x_0} - x_0 \bar{\eta} + \frac{x_0}{2}\left(\eta_a + \eta_b\right) + \frac{x_0^2}{3}\left(\eta_a' - \eta_b'\right) \\ & + \frac{x_0}{2} \int_{-1}^{+1} \left[\frac{\eta\left(\ell + dy\right) + \eta\left(\ell - dy\right) - \eta_a - \eta_b}{1 - y^2} \right] \mathrm{d}y \Bigg\} + O\left(\eta_0^2, \eta_0^2 k_0, \eta_0^2 k_0^2\right), \end{aligned} \tag{3.5}$$

upon linearization. Using (2.1) in the equation above we obtain

$$\begin{aligned} M_0 = \frac{x_0^2}{3} \Bigg\{ & 1 + 2\frac{\varepsilon}{x_0} + \frac{\eta_0 x_0}{\sqrt{N}} \sum_{m=1}^{N} \left(\alpha_m \sin k_m \ell + \beta_m \cos k_m \ell\right) \Bigg(\cos k_m x_0 - \frac{\sin k_m x_0}{k_m x_0} \\ & - \frac{2}{3} x_0 k_m \sin k_m x_0 + \int_{-1}^{+1} \frac{\cos k_m x_0 y - \cos k_m x_0}{1 - y^2} \mathrm{d}y \Bigg) \Bigg\} + O\left(\eta_0^2, \eta_0^2 k_0, \eta_0^2 k_0^2\right), \end{aligned} \tag{3.6}$$

where $k_m = k_0 m/N$. The rest of the computations are carried out in a similar manner. By neglecting the higher-order terms in η_0 we obtain at the end a stochastic differential equation for ε of the form

$$\dot{\varepsilon} + A\left(t\right)\varepsilon = \frac{\eta_0}{\sqrt{N}} \sum_{m=1}^{N} \left(\alpha_m \sin k_m \ell + \beta_m \cos k_m \ell\right) B\left(t, k_m x_0\right), \tag{3.7}$$

where

$$\begin{aligned} A\left(t\right) &= \frac{1}{x_0 \ln \dfrac{2x_0}{\lambda e^2}} \left(\dot{x}_0 + \frac{54}{x_0^6}\right), \\ B\left(t, \xi\left(t\right)\right) &= \frac{x_0}{\ln \dfrac{2x_0}{\lambda e^2}} \left\{ \frac{27}{x_0^6} \left(\operatorname{sinc}\xi - \cos\xi - \frac{1}{3}\xi \sin\xi\right) \right. \\ &\quad \left. + \dot{x}_0 \left[\left(\xi \sin\xi - \cos\xi\right) \operatorname{Cin} 2\xi + \left(\xi \cos\xi + \sin\xi\right) \operatorname{Si} 2\xi - 3\xi \sin\xi\right] \right\}. \end{aligned}$$

Here we set:

$$\begin{aligned} \operatorname{sinc} x &= \frac{\sin x}{x}, \\ \operatorname{Si} x &= \int_0^x \operatorname{sinc} x' \,\mathrm{d}x', \\ \operatorname{Cin} x &= \int_0^x \frac{1 - \cos x'}{x'} \,\mathrm{d}x', \end{aligned}$$

corresponding to the cardinal sine function, sine and cosine integrals, respectively (Abramowitz & Stegun 1964). Since (3.7) is linear in ε, we can obtain the following explicit solution:

$$\varepsilon\left(t\right) = \frac{\eta_0}{\sqrt{N}} \sum_{m=1}^{N} \int_0^t \left(\alpha_m \sin k_m \ell + \beta_m \cos k_m \ell\right) B\left(t', k_m x_0\right) \exp\left(-\int_{t'}^{t} A\left(t''\right) \,\mathrm{d}t''\right) \mathrm{d}t'. \tag{3.8}$$

For the droplet shift we obtain the stochastic differential equation

$$\dot{\ell} = \frac{\eta_0}{\sqrt{N}} \sum_{m=1}^{N} \left(\alpha_m \cos k_m \ell - \beta_m \sin k_m \ell\right) C\left(t, k_m x_0\right), \tag{3.9}$$

where, again, the higher order terms are neglected and:

$$C\left(t,\xi\left(t\right)\right)=\frac{x_0}{\ln\frac{2x_0}{\lambda}}\left\{\frac{9}{x_0^6}\left(\xi\cos\xi-\sin\xi\right)\right.$$
$$\left.+\,\dot{x}_0\left[\xi\left(\frac{7}{3}-\mathrm{Cin}\,2\xi\right)\cos\xi+\left(\xi\,\mathrm{Si}\,2\xi-\frac{7}{3}\right)\sin\xi\right]\right\}.$$

It is clear that in the above system of differential equations, (3.7) and (3.9), the time dependence enters $A\left(t,\xi\left(t\right)\right)$, $B\left(t,\xi\left(t\right)\right)$ and $C\left(t,\xi\left(t\right)\right)$ through $x_0\left(t\right)$ and its time derivative.

Evidently, the solution to (3.9) cannot be given in explicit form. However, since at $t=0$ we have that $\ell=0$, we may obtain its early-time behavior by expanding the trigonometric functions for small ℓ which leads to:

$$\dot{\ell}=\frac{\eta_0}{\sqrt{N}}\sum_{m=1}^{N}\left(\alpha_m-\beta_m k_m\ell\right)C\left(t,k_m x_0\right)+O\left(\ell^2\right). \tag{3.10}$$

By neglecting the higher-order terms, we obtain a linear differential equation for ℓ that may be solved explicitly to obtain:

$$\ell\left(t\right)=\frac{\eta_0}{\sqrt{N}}\sum_{m=1}^{N}\int_0^t\alpha_m C\left(t',k_m x_0\right)\exp\left(-\frac{\eta_0}{\sqrt{N}}\sum_{n=1}^{N}\int_{t'}^{t}\beta_n k_n C\left(t'',k_n x_0\right)\,\mathrm{d}t''\right)\,\mathrm{d}t'. \tag{3.11}$$

Similarly, (3.8) becomes:

$$\varepsilon\left(t\right)=\frac{\eta_0}{\sqrt{N}}\sum_{m=1}^{N}\int_0^t\left(\alpha_m k_m\ell+\beta_m\right)B\left(t',k_m x_0\right)\exp\left(-\int_{t'}^{t}A\left(t''\right)\,\mathrm{d}t''\right)\,\mathrm{d}t'. \tag{3.12}$$

The analysis that follows is based on the system of differential equations (3.2), (3.7) and (3.9) and aims to characterize the statistics of ε and ℓ. Our theoretical predictions will be compared with numerical solutions to the IDEs in (2.5) by considering typically 2×10^4 realizations from each substrate family. At $t=0$, we take $x_0(0)=1$, $\varepsilon(0)=0$ and $\ell(0)=0$. Given also the generally weak dependence of the dynamics on the slip length (Hocking 1983), in all computations we fixed $\lambda=10^{-4}$ as well as the static contact angle $\alpha_s=10^\circ$ in order to focus only on the effects of substrate topography. The value of

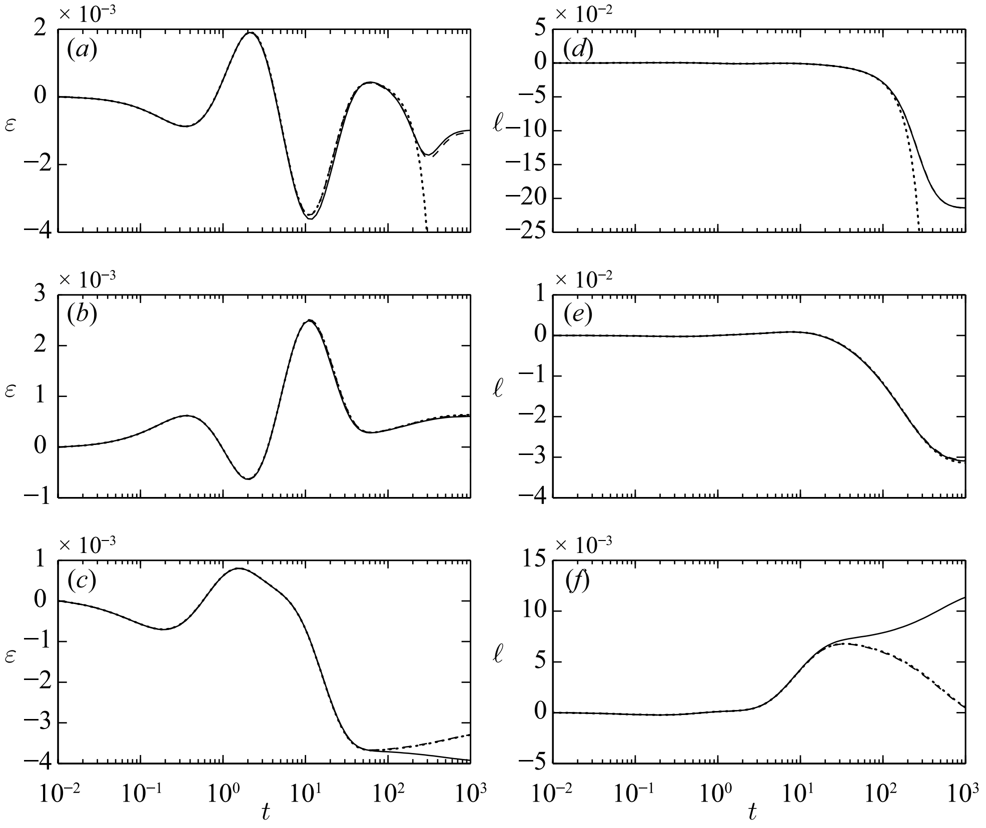

FIGURE 1. Time-evolution of ε and ℓ for $\eta_0 = 5 \times 10^{-4}$ and $k_0 = 15$ for 3 substrate realizations comparing the solutions to the IDEs (solid lines), (3.1), the solutions to the linearized equations (dashed lines), (3.7) and (3.9), and the early-time approximation (dotted lines), (3.11) and (3.12). The plots in (*a*-*c*) show curves of $\varepsilon(t)$ for each of the 3 random substrate realizations and those in (*d*-*f*) show the corresponding curves for $\ell(t)$.

the static contact angle in particular, is not expected to play an important role. It must be small to conform with the long-wave expansion and besides, it enters the boundary conditions (2.4) as α_s^2.

Typical evolution curves for $\varepsilon(t)$ and $\ell(t)$ are shown in figure 1 for 3 random substrate realizations with $\eta_0 = 5 \times 10^{-4}$ and $k_0 = 15$. The plots in figure 1(*a*-*c*) depict the curves of ε as a function of t for each of these substrate realizations and the plots in figure 1(*d*-*f*) show the corresponding evolution curves for ℓ. The solid lines are the solutions to the system of IDEs, (3.1), the dashed curves are the solutions to the linerarized equations, (3.8) and (3.9), whereas the dotted lines correspond to the early-time asymptotic curves, (3.11) and (3.12). Provided that (3.3) is valid, our linearized theory typically yields excellent results, especially at the onset of spreading. In the majority of our random simulations, we observe behaviors similar to plots (a) and (d), where we notice an overall good agreement for all times for the linearized equations, but the early-time asymptotics fail to capture the long-time behavior. It also quite common to find substrate realizations for which the agreement is excellent for all times, even for the early-time asymptotics, as shown in plots (b) and (e), where all 3 curves are nearly indistinguishable. However, in some rare cases illustrated by plots (c) and (f), our theory fails to predict the behavior at long-times and there is a clear deviation towards different equilibria. This is possibly due to the nonlinear interplay of our small parameter, $\eta_0 k_0^2$, with $\dot{x}_0$ when the latter is also small. However, since such cases are not as common as the other two cases, we do not believe that they can affect the overall statistics and for this reason we did not deem it necessary to exclude such situations. Having verified the generally excellent performance of our linear theory, we proceed to examine the statistics of ℓ, since its leading order dynamics does not depend on ε, as suggested by (3.9).

4. Droplet shift dynamics

As we mentioned above, equation (3.9) cannot be solved analytically and a theoretical assessment of the statistics of ℓ for all times is not possible. As a matter of fact, we are bound to encounter similar difficulties in assessing the statistical properties of ℓ as we did for its static equilibria in Part 1. Nevertheless, it is still possible to examine analytically the early-/long-time asymptotics of equation (3.9).

Due to symmetry, we expect that $\langle \ell\,(t) \rangle = 0 \ \forall t$, since the droplet should not preferentially slide on either side of the topography with respect to our chosen origin. Clearly the effects of the substrate characteristics on wetting do not depend explicitly on the statistics of ℓ, since only the statistics of the droplet radius is needed to calculate, for example, an apparent contact angle. However, the droplet shift is expected to influence wetting indirectly as the dependence of ε on ℓ in (3.7) suggests.

While considering the statics in Part 1, we concluded that the statistics of ℓ does not depend on η_0. We note from equation (3.9), however, that the speed at which the droplet slides is influenced by η_0. In fact, due to the linearity of (3.9) on η_0 the equilibrium tends to be attained at a faster rate when the topography amplitude increases.

Hence, at the onset we see from (3.10) that ℓ is given as an infinite sum of random variables with well prescribed moments and by the Central Limit Theorem (Breiman 1992), it is therefore well approximated as a normal variable. At later times, $\dot{\ell} \to 0$ and (3.10) predicts that ℓ approaches a ratio of two normal variables, i.e. a Cauchy random variable, whose mean and variance are not defined. We have seen in Part 1, however, that the equilibria of ℓ have a well-defined variance, albeit with a probability density that cannot be determined analytically. Hence, we can assess the region of validity of (3.11) by computing the variance of ℓ and compare it with results from numerical experiments. Consider:

$$\ell^2 = \frac{\eta_0^2}{N} \sum_{q=1}^{N} \sum_{m=1}^{N} \alpha_q \alpha_m \int_0^t \int_0^t C\left(t', k_m x_0\right) C\left(t'', k_n x_0\right)$$
$$\times \exp\left(-\frac{\eta_0}{\sqrt{N}} \sum_{n=1}^{N} \beta_n \left[\int_{t'}^{t} k_q C\left(t''', k_n x_0\right)\, \mathrm{d}t''' + \int_{t''}^{t} k_n C\left(t''', k_n x_0\right)\, \mathrm{d}t'''\right]\right) \mathrm{d}t' \mathrm{d}t''.$$

By taking the mean, we can suppress the summation with respect to q due to the mutual independence of the α_m's so that

$$\begin{aligned}\mathrm{Var}\left[\ell\right] = \left\langle \ell^2 \right\rangle = \frac{\eta_0^2}{N} \sum_{m=1}^{N} \int_0^t \int_0^t C\left(t', k_m x_0\right) C\left(t'', k_q x_0\right) \\ \times \exp\left(\frac{\eta_0^2}{2N} \sum_{n=1}^{N} \left[\int_{t'}^{t} k_n C\left(t''', k_n x_0\right) \, \mathrm{d}t''' + \int_{t''}^{t} k_n C\left(t''', k_n x_0\right) \, \mathrm{d}t''' \right]^2 \right) \mathrm{d}t' \mathrm{d}t'',\end{aligned}$$

where the mean of the exponential term is found using $\left\langle e^X \right\rangle = e^{\sigma_X^2/2}$, for X being a zero-mean normal variable with variance σ_X^2. Conversion of the Riemann sums into integrals gives the variance of ℓ at early times

$$\begin{aligned}\mathrm{Var}\left[\ell\right] = \eta_0^2 \int_0^1 \int_0^t \int_0^t C\left(t', k_0 x_0 y\right) C\left(t'', k_0 x_0 y\right) \\ \times \exp\left(\frac{\eta_0^2 k_0^2}{2} \int_0^1 \left[D\left(t', q; t\right) + D\left(t'', q; t\right) \right]^2 \mathrm{d}q \right) \mathrm{d}t' \mathrm{d}t'',\end{aligned} \tag{4.1}$$

where the functional D is given by:

$$D\left(\tau, q; t\right) = \int_{\tau}^{t} q C\left(t', q k_0 x_0\left(t'\right)\right) \mathrm{d}t'.$$

Figure 2 depicts the evolution of $\sigma_\ell = \sqrt{\mathrm{Var}\left[\ell\right]}$ as computed from numerical experiments, together with the early-time behavior predicted by (4.1) for $\eta_0 = 5 \times 10^{-4}$ and $k_0 = 10$, 20, 30 and 40. We note that depending on the value of k_0 the agreement between the linear theory and the numerics can be excellent even up to $t \sim O\left(10^2\right)$; after that time the theoretically predicted variance goes to infinity in accord with our earlier discussion that the linearized equation predicts a Cauchy variable in the long-time limit. For intermediate times, it is impossible to theoretically predict any of the statistical properties of ℓ and we can only resort to a numerical study. Naturally, the tendency of the droplet to slide along the topographical features is reduced as k_0 increases. This behavior may be inferred from figure 2, where we see that at the end of computation, at $t = 380$, σ_ℓ is closer to saturating for $k_0 = 40$ compared to $k_0 = 10$ which is still growing.

In the long-time limit, where $\dot{\ell} \to 0$ and $\ell \to \ell_\infty$, we obtain the following equation for

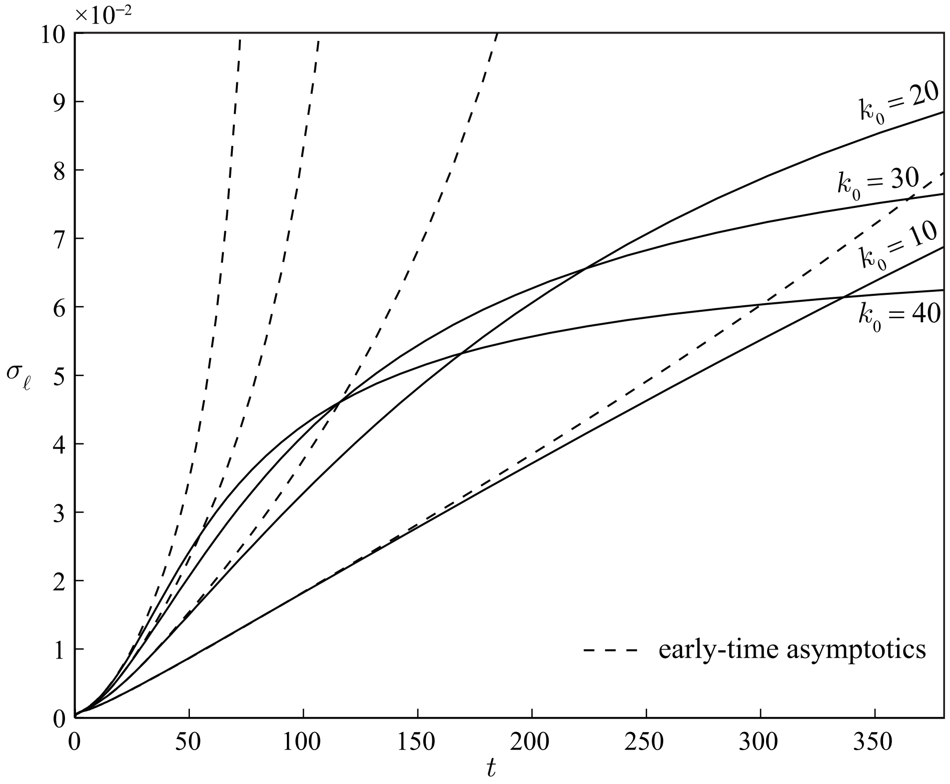

FIGURE 2. Time evolution of σ_ℓ for $\eta_0 = 5 \times 10^{-4}$ and $k_0 = 10$, 20, 30 and 40. The solid lines correspond to numerical experiments, whereas the dotted lines to the early-time asymptotics predicted by (4.1).

the droplet shift at equilibrium,

$$\sum_{m=1}^{N} \left(\alpha_m \cos k_m \ell_\infty - \beta_m \sin k_m \ell_\infty\right) G\left(k_m \sqrt{3}\right) = 0, \tag{4.2}$$

which is identical to equation (3.11) obtained in Part 1 for the droplet statics (as in Part 1, we set $G(\xi) = \xi \cos \xi - \sin \xi$). As we also pointed out in Part 1, (4.2) admits infinitely many solutions as $N \to \infty$. But now we are dealing with a dynamical system and where contrary to the statics we have an evolution from $\ell = 0$ to ℓ_∞. Hence, we are not only interested in a solution to (4.2) that is *closest* to $\ell = 0$, but also in a solution that corresponds to a stable equilibrium. Again this is is reminiscent of a first passage problem, but we have the additional constraint that the equilibrium ℓ_∞ must also be stable. To find conditions for the stability of this equilibrium, we introduce in (3.9) $\ell = \ell_\infty + \tilde{\ell}$ where $\tilde{\ell}$ a small perturbation. Doing so yields the linearized system:

$$\dot{\tilde{\ell}} = -\frac{\eta_0}{\sqrt{3}\ln\frac{2\sqrt{3}}{\lambda}}\left[\sum_{m=1}^{N} k_m\left(\alpha_m \sin k_m\ell_\infty + \beta_m \cos k_m\ell_\infty\right) G\left(k_m\sqrt{3}\right)\right]\tilde{\ell}.$$

Linear stability of the equilibrium $\ell = \ell_\infty$ requires that

$$\sum_{m=1}^{N} k_m\left(\alpha_m \sin k_m\ell_\infty + \beta_m \cos k_m\ell_\infty\right) G\left(k_m\sqrt{3}\right) > 0, \tag{4.3}$$

which should also hold for the ensemble average. Hence, we anticipate that the validity of an ensemble average of the above inequality is guaranteed if we have,

$$\langle \alpha_m \sin k_m\ell_\infty + \beta_m \cos k_m\ell_\infty \rangle \propto \frac{G\left(k_m\sqrt{3}\right)}{\sqrt{N}},$$

so that the summands in (4.3) are all positive. A rigorous theory to support the above claim is presently lacking but our numerical experiments suggest that, provided (3.3) holds, we have:

$$\langle \alpha_m \sin k_m\ell_\infty + \beta_m \cos k_m\ell_\infty \rangle \approx \sqrt{\frac{3}{N}}\frac{G\left(k_m\sqrt{3}\right)}{k_0}. \tag{4.4}$$

The inverse square root dependence on the number of harmonics comes as no surprise since as N increases, the final value of ℓ_∞ becomes "less dependent" on the individual α_m and β_m. At this stage it is crucial not to take $N \to \infty$ in which case the right-hand-side of (4.4) vanishes, because this relation has important implications in characterizing wetting on random substrates, as it is responsible for a non-zero $\langle\varepsilon\rangle$. To demonstrate the validity of this semi-analytical result, we depict in figure 3 plots of the mean of $\alpha_m \sin k_m\ell_\infty + \beta_m \cos k_m\ell_\infty$ as a function of m/N. In figure 3(a), $N = 900$ harmonics were used with $\eta_0 = 10^{-3}$ and $k_0 = 15$ and in figure 3(b), $N = 800$ with $\eta_0 = 10^{-3}$ and $k_0 = 40$. Evidently, our numerical experiments (thin lines) closely follow (4.4) (thick lines), even for $k_0 = 40$, where, strictly speaking, (3.3) does not hold. The fluctuations, which appear

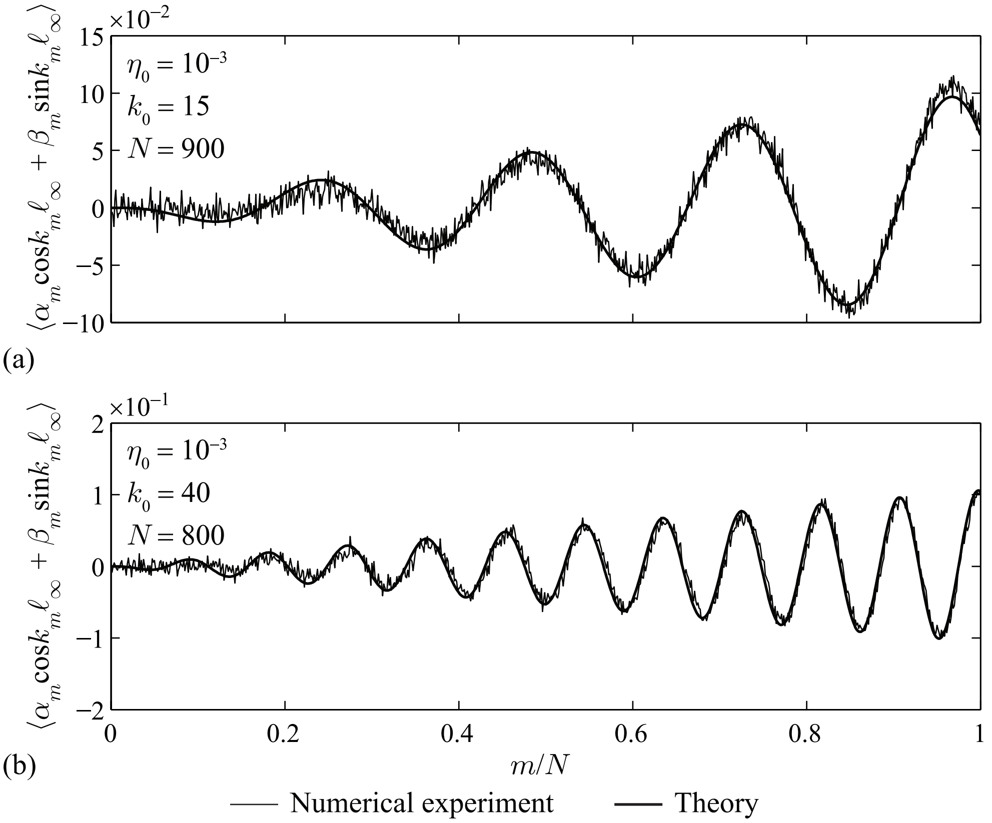

FIGURE 3. Comparison of $\langle \alpha_m \sin k_m \ell_\infty + \beta_m \cos k_m \ell_\infty \rangle$ obtained from experiments (thin lines) and the semi-analytical result (4.4) (thick lines) for substrate families with (*a*) $\eta_0 = 10^{-3}$, $k_0 = 15$, $N = 900$ and (*b*) $\eta_0 = 10^{-3}$, $k_0 = 40$ and $N = 800$.

to persist regardless of the size of N, may be possibly attributed to unavoidable roundoff errors in our computations.

The probability density function of ℓ_∞ cannot be predicted analytically, but can be nevertheless approximated via Padé approximants as discussed in Part 1. The computation of the variance of ℓ_∞ is performed in a manner similar to that in Part 1. We expect that the variance scales with $\langle \Delta \ell \rangle^2$, where $\langle \Delta \ell \rangle$ is the mean distance between zeros, given by (4.5) of Part 1. Since on average, a stable equilibrium is expected to be found within

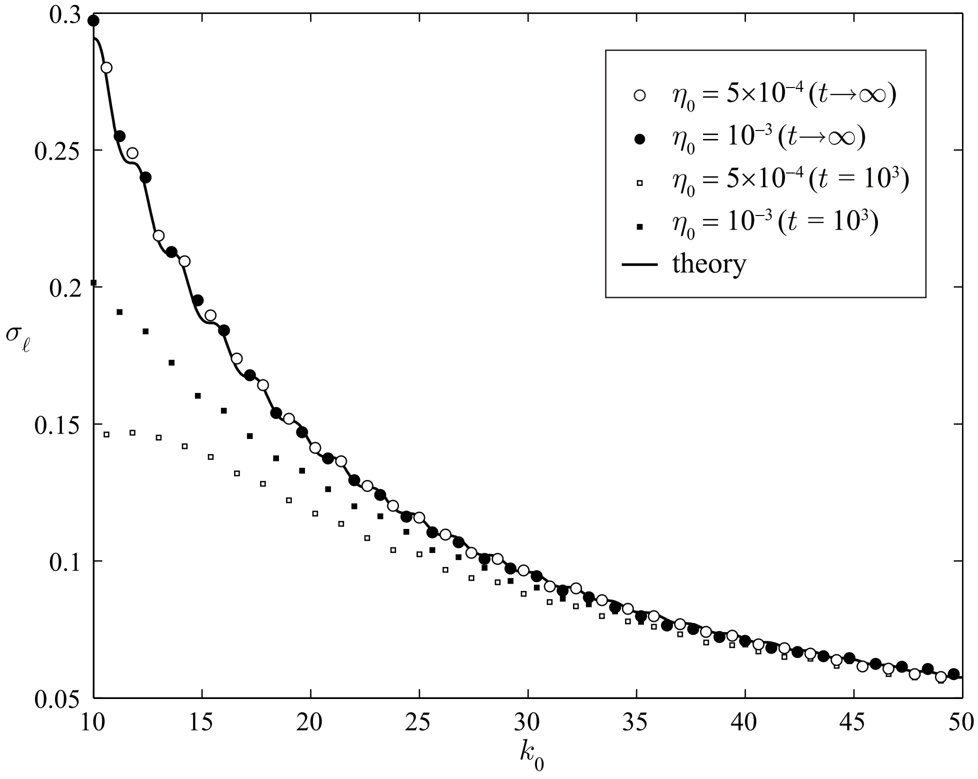

FIGURE 4. Variation of σ_ℓ as a function of k_0 at equilibrium (circles) and at time $t = 1000$ (squares) together with the equilibrium predicted by (4.5). The open and filled symbols correspond to $\eta_0 = 5 \times 10^{-4}$ and $\eta_0 = 10^{-3}$, respectively. In the long-time limit σ_ℓ becomes independent of η_0.

a distance $\langle \Delta\ell \rangle$ from the origin, we can also argue that

$$\sigma^2_{\ell_\infty} = \mathrm{Var}\left[\ell_\infty\right] = \frac{1}{2}\left\langle \Delta\ell \right\rangle^2 \sim \frac{5\pi^2}{6k_0^2}\left[1 - 2\,\mathrm{sinc}\left(2k_0\sqrt{3}\right)\right] + O\left(k_0^{-4}\right), \tag{4.5}$$

in the limit $k_0 \gg 1$. It is important to note that $\mathrm{Var}\left[\ell_\infty\right]$ is 4 times larger than the one obtained from statics considerations. This is attributed to the fact that, on average half of the equilibria considered are unstable, whereas in a dynamic setting we are seeking only the stable equilibria. The overall qualitative behavior is that the droplet slides less as the lengthscale of substrate variations decrease. Such behavior is confirmed in figure 4 where we show the theoretically predicted σ_{ℓ_∞} as a function of k_0 together with numerical experiments for substrate families with $\eta_0 = 10^{-3}$ (filled circles) and $\eta_0 = 5 \times 10^{-4}$ (open circles). In figure 4 we also depict with filled and open squares the corresponding σ_ℓ at time $t = 1000$. For smaller η_0, the approach to equilibrium is slower compared to that for larger values of η_0, but as $t \to \infty$, σ_ℓ eventually becomes independent of η_0. Finally, it is worth noting that our numerical experiments also show that the veracity of (4.5) may extend beyond its regime of validity imposed by (3.3).

5. Contact line fluctuation dynamics

The dynamics of contact line fluctuations can be used to asses the effect of the substrate features on wetting. This can be quantified through the apparent contact angle, θ_{app}, given by

$$\theta_{\text{app}} = \frac{3}{(x_0 + \varepsilon)^2} = \theta_{\text{flat}} \left(1 - 2\frac{\varepsilon}{x_0} \right) + O\left(\varepsilon^2 / x_0^2\right), \tag{5.1}$$

where $\theta_{\text{flat}} = 3/x_0^2$ corresponds to the apparent contact angle for a droplet on an ideally flat substrate. As we already pointed out in §4, the dynamics of ℓ is required in the computations for ε, because it appears in its evolution equation, (3.8).

The Central Limit Theorem is expected to apply in (3.8) and through a similar reasoning as the one offered in §4 for (3.11), we may conclude that $\varepsilon(t)$ is adequately approximated by a normal variable for all t with a probability density function

$$p_\varepsilon(\epsilon) = \frac{1}{\sqrt{2\pi\sigma_\varepsilon^2}} \exp\left(-\frac{(\epsilon - \mu_\varepsilon)^2}{2\sigma_\varepsilon^2} \right),$$

where μ_ε corresponds to its mean and σ_ε^2 to its variance. Hence the statistics of ε is completely determined by μ_ε and σ_ε^2. However, the dependence of ε on ℓ complicates matters considerably.

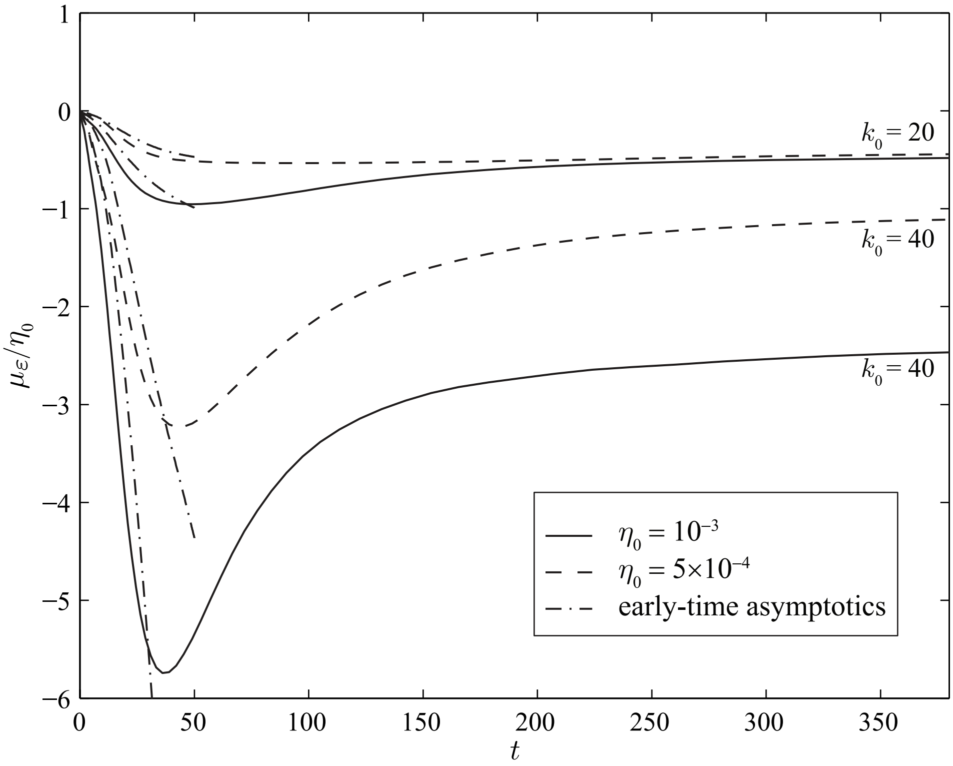

FIGURE 5. Evolution of μ_ϵ/η_0 as a function of t for substrate families with $\eta_0 = 10^{-3}$ (solid lines) and $\eta_0 = 5 \times 10^{-4}$ (dashed lines). When $k_0 = 20$, μ_ϵ/η_0 approaches a common value in the long-time limit for both amplitudes.

5.1. *Mean of contact line fluctuations*

The present theory cannot predict the time evolution of μ_ε, because to do so we need to determine $\langle \alpha_m \sin k_m\ell + \beta_m \cos k_m\ell\rangle$ as a function of t, a task that cannot be carried out analytically. However, we can deduce a differential equation for the early-time behavior of μ_ε, using the early-time behavior of $\ell\,(t)$, prescribed by (3.11). Since at the onset ℓ is small, we expand (3.7) for small ℓ and use (3.11) to finally obtain

$$\dot{\mu}_\varepsilon + A\,(t)\,\mu_\varepsilon = \eta_0^2 k_0 \int_0^1 yB\,(t, k_0x_0y) \\ \times \int_0^t C\,(t', k_0x_0y) \exp\left(\frac{\eta_0^2 k_0^2}{2}\int_0^1 \left[q\int_{t'}^t C\,(\tau, k_0x_0q)\;\mathrm{d}\tau\right]^2 \mathrm{d}q\right) \mathrm{d}t'\,\mathrm{d}y,$$

upon taking an ensemble average of all substrate realizations. Again, this is a linear equation whose solution may be written explicitly as:

$$\mu_\varepsilon\left(t\right)=\eta_0^2 k_0\int_0^t \exp\left[-\int_{t'}^t A\left(s\right)\,\mathrm{d}s\right]\int_0^{t'}\exp\left(\frac{\eta_0^2 k_0^2}{2}\int_0^1\left[q\int_{t''}^{t'}C\left(\tau,k_0x_0q\right)\,\mathrm{d}\tau\right]^2\mathrm{d}q\right)$$
$$\times\int_0^1 yB\left(t',k_0x_0y\right)C\left(t'',k_0x_0y\right)\,\mathrm{d}y\,\mathrm{d}t''\,\mathrm{d}t'. \tag{5.2}$$

For arbitrary t, we can determine the dynamic variation of μ_ε via numerical experiments. In figure 5 we plot μ_ε/η_0 as a function of t, for $0\leqslant t\leqslant 380$, for substrate families with $\eta_0 = 10^{-3}$ (solid lines) and $\eta_0 = 5\times10^{-4}$ (dashed lines) for two characteristic wavenumbers $k_0 = 20$ and $k_0 = 40$. We note that the approach towards equilibrium need not be monotonic. For some of these curves we observe a rapid change in μ_ϵ for relatively small t prior to relaxation to equilibrium for larger t. More importantly, we see that when $k_0 = 20$, μ_ε/η_0 approaches a common value as $t\to\infty$. In figure 5 we also plot the corresponding early-time asymptotics (dash-dotted lines), given by (5.2). Surprisingly, the agreement between our theory and the result from the numerical experiments appears to be somewhat weak, despite the fact that we found in §3 that the spreading dynamics at the onset is nearly indistinguishable from the results of our linear theory. This inconsistency is due to the limited number of substrate realizations we considered in this particular calculation (2×10^4). In fact, we have found compelling numerical evidence that the convergence to the mean is extremely slow compared to the convergence to the second moments and hence a much larger number of substrate realizations is required for the mean to converge to the theoretically predicted curves.

In the long-time limit, which is of great importance when obtaining the mean of the apparent contact angle at equilibrium, $\langle\theta_{\mathrm{app}}\rangle$, we can use the semi-analytical expression for $\langle\alpha_m\sin k_m\ell_\infty+\beta_m\cos k_m\ell_\infty\rangle$ in (4.4). Conversion of the Riemann sum into an integral

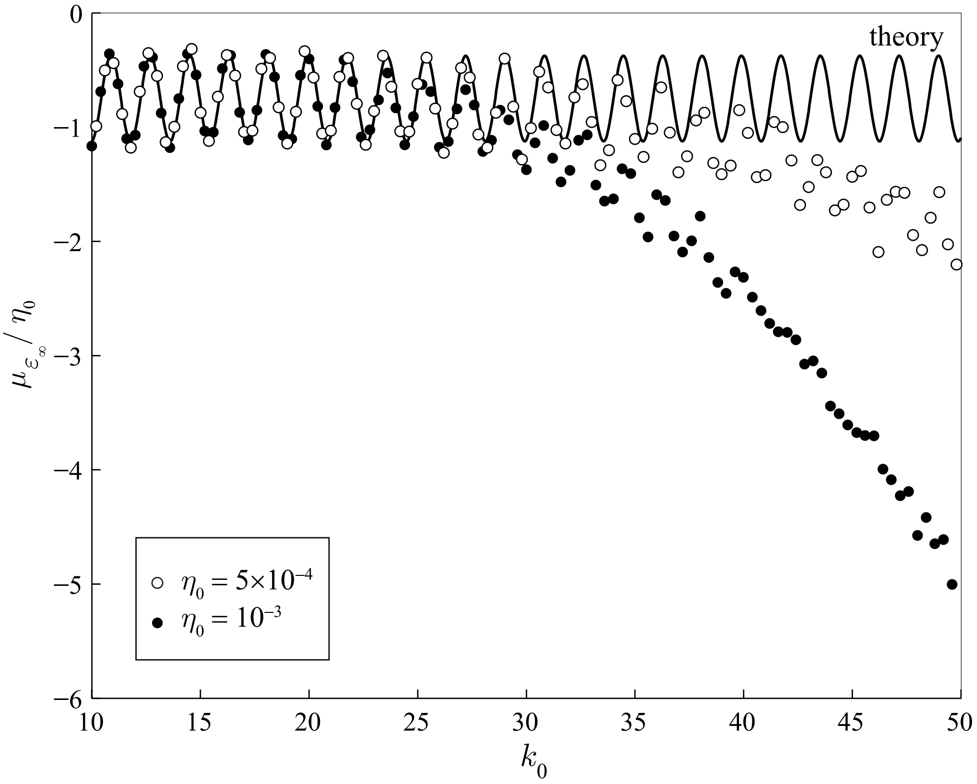

FIGURE 6. Variation of $\mu_{\varepsilon_\infty}/\eta_0$ as a function of k_0 for substrate families with $\eta_0 = 5 \times 10^{-4}$ (open circles) and $\eta_0 = 10^{-3}$ (filled circles) together with the corresponding theoretical curve, (5.3). Deviations occur for larger k_0, as the perturbation condition, (3.3), no longer holds.

yields

$$\mu_{\varepsilon_\infty} \approx \frac{\sqrt{3}\eta_0}{2k_0} \int_0^1 G\left(k_0 y\sqrt{3}\right) F\left(k_0 y\sqrt{3}\right)\, \mathrm{d}y,$$

where as in Part 1, $F(\xi) = 3\,\mathrm{sinc}\,\xi - 3\cos\xi - \xi\sin\xi$. The above integral can be computed analytically to obtain:

$$\mu_{\varepsilon_\infty} \approx -\frac{3\eta_0}{8}\left(2 - \cos 2\sqrt{3}k_0\right) - \frac{15\eta_0}{4}\,\mathrm{sinc}\,2k_0\sqrt{3} + \frac{\eta_0}{8}\left(17\sin^2 k_0\sqrt{3} - 6\,\mathrm{Cin}\,2k_0\sqrt{3}\right). \tag{5.3}$$

In the limit $k_0 \gg 1$, μ_{ε_∞} has the asymptotic expansion

$$\mu_{\varepsilon_\infty} \sim -\frac{3\eta_0}{8}\left(2 - \cos 2\sqrt{3}k_0\right) + O\left(\eta_0 k_0^{-1}\right), \tag{5.4}$$

which implies that the mean contact line fluctuation is negative over the regime of interest and also explains the earlier observation in figure 5 that for $k_0 = 20$, the curves for μ_ϵ/η_0 when $\eta_0 = 10^{-3}$ and $\eta_0 = 5 \times 10^{-4}$ share a common limit. Using (5.1) it can be shown that the ratio of the mean equilibrium apparent contact angle for a droplet on a rough substrate over the apparent contact angle on a flat substrate is given by:

$$\frac{\langle\theta_{\mathrm{app}}\rangle}{\theta_{\mathrm{flat}}} \sim 1 + \frac{\eta_0\sqrt{3}}{4}\left(2 - \cos 2\sqrt{3}k_0\right) + O\left(\eta_0 k_0^{-1}\right).$$

This result suggests that $\langle\theta_{\mathrm{app}}\rangle > \theta_{\mathrm{flat}}$, i.e. wetting is ultimately reduced linearly in η_0 over the regime where the perturbation expansion is valid, having also an oscillatory behavior as k_0 varies.

Figure 6 depicts a plot of (5.3) as a function of k_0 together with the means obtained from numerical simulations for substrates with various substrate families, with two different $\eta_0 = 10^{-3}$ and $\eta_0 = 5 \times 10^{-4}$. For k_0 in the region $\sim [10, 15]$, the agreement between the semi-analytic approximation and the numerical experiments is excellent, but as the substrate becomes more rough so that $\eta_0 k_0^2 \ll 1$ is no longer valid, there is a clear deviation towards a progressive reduction of the mean droplet radius. Most importantly, the present analysis demonstrates that, by taking into account the dynamics, substrate roughness ultimately reduces wetting on average. Even though such behavior appears to contradict Wenzel's law, which predicts wetting enhancement for rough substrates, it signifies the fact that the droplet has to overcome the energy barriers that separate the multiple equilibrium droplet states. In other words, in a dynamic setting the droplet can get "trapped" in an equilibrium state prior to reaching a Wenzel state. This effect is demonstrated in the recent experiments of Chung *et al.* (2007), where it was found that spreading in a direction perpendicular to the grooves indeed violates Wenzel's law. It is further supported by the work of Cox (1983) on wedge equilibria over three-dimensional rough substrates, who postulated that roughness-induced wetting enhancement is due to

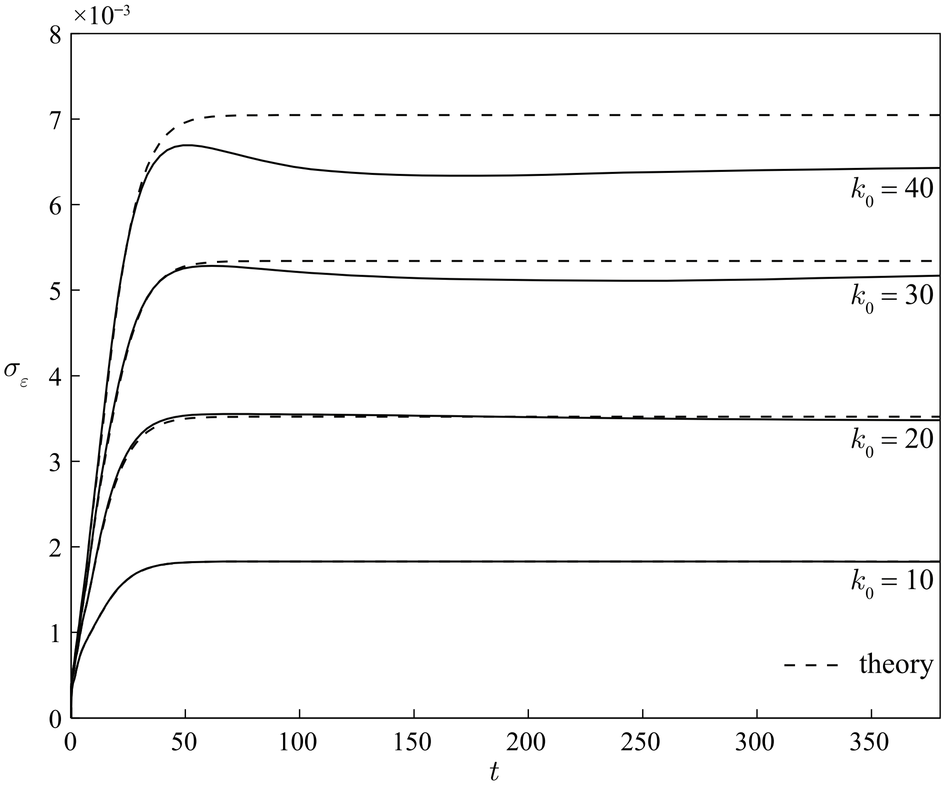

FIGURE 7. Time evolution of σ_ε for $\eta_0 = 5 \times 10^{-4}$ and $k_0 = 10$, 20, 30 and 40. The solid lines correspond to numerical experiments, whereas the dotted lines to the linear theory, (5.6). When $k_0 = 10$, there is perfect agreement of the theory and numerical experiment.

a higher order effect, which manifests itself when spreading does not occur in a direction perpendicular to the substrate grooves.

5.2. *Variance of fluctuations*

The variance of ε, σ_ε^2, is more easily determined for all times compared to its mean, provided that we make some simplifying assumptions. In §4 we argued that as the number of harmonics increases, ℓ becomes less dependent on the α_m's and β_m's. Taking this into account when considering the variance of ε, we have

$$\sigma_\varepsilon^2 \approx \frac{\eta_0^2}{N} \sum_{m=1}^{N} \left\langle \alpha_m^2 \right\rangle \left\langle \left[\int_0^t \sin k_m \ell \, B\left(t', k_m x_0\right) \exp\left(- \int_{t'}^{t} A\left(t''\right) \, \mathrm{d}t'' \right) \mathrm{d}t' \right]^2 \right\rangle$$
$$+ \left\langle \beta_m^2 \right\rangle \left\langle \left[\int_0^t \cos k_n \ell \, B\left(t', k_n x_0\right) \exp\left(- \int_{t'}^{t} A\left(t''\right) \, \mathrm{d}t'' \right) \mathrm{d}t' \right]^2 \right\rangle, \quad (5.5)$$

where the cross-terms were neglected on the basis of the mutual independence of the α_m's and β_m's. In §4 we noted that the lengthscale over which ℓ varies is long compared to ε, due to the small characteristic amplitude of the topography. Thus, at least for small t, we may take the trigonometric functions of ℓ outside the integrals with respect to t'. Doing so we obtain an approximate expression for σ_ε^2,

$$\sigma_\varepsilon^2\left(t\right) \approx \eta_0^2 \int_0^1 \left[\int_0^t B\left(t', y k_0 x_0\right) \exp\left(- \int_{t'}^{t} A\left(t''\right) \, \mathrm{d}t'' \right) \mathrm{d}t' \right]^2 \mathrm{d}y, \quad (5.6)$$

where, again, the Riemann sum is converted into an integral as $N \to \infty$.

Figure 7 shows plots of σ_ε as a function of time for $\eta_0 = 5 \times 10^{-4}$ and $k_0 = 10$, 20, 30 and 40. We observe that, despite our simplifying assumptions, the agreement between the theoretically predicted curves and the ones obtained from numerical experiments is quite good, especially for small times. For $k_0 = 10$ the two curves are practically indistinguishable, but as expected the agreement tends to degrade as (3.3) no longer holds. It is worth noting that the timescale over which σ_ε saturates is independent of k_0, compared to σ_ℓ of figure 2, which is highly dependent on k_0. Finally, these timescales are much shorter for σ_ε compared to σ_ℓ, which signifies the fact that when a droplet spreads on a parallel-grooved substrate, it may spend more time sliding along the topographical features than spreading. Thus the droplet quickly spreads so that its free-surface nearly attains its equilibrium shape, but reaching the actual equilibrium takes a longer time due to the sliding motion. Nevertheless, the rate at which this happens is quite small and in reality the slightest bump on the topography can stop the already slowly moving droplet.

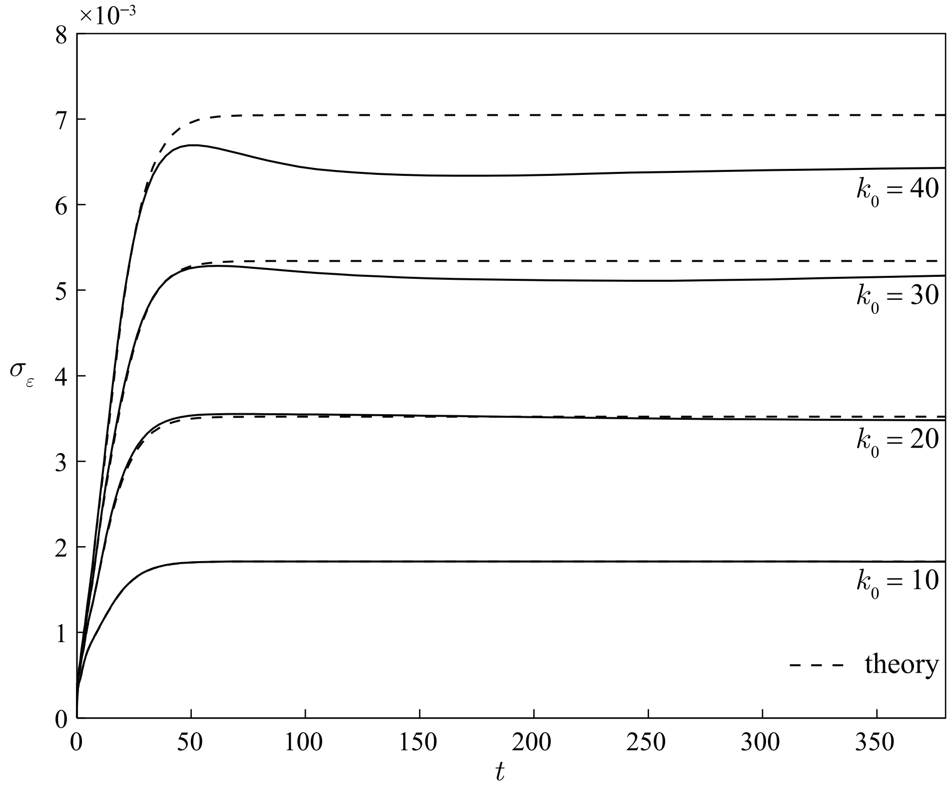

FIGURE 8. Variation of σ_ε at equilibrium as a function of k_0 for substrate families with $\eta_0 = 5 \times 10^{-4}$ (open circles) and $\eta_0 = 10^{-3}$ (filled circles) together with the corresponding theoretical curve, (5.7). Agreement degrades as k_0 icreases so that (3.3) is no longer invalid.

In the long-time limit, the variance predicted by (5.6) is identical to (5.2) obtained in Part 1 for the statics, whose asymptotic behavior is

$$\sigma^2_{\varepsilon_\infty} \sim \frac{\eta_0^2 k_0^2}{8} \left(1 - 3\,\mathrm{sinc}\,2\sqrt{3}k_0\right) + O\left(\eta_0^2\right), \tag{5.7}$$

when $k_0 \gg 1$. The theoretically predicted $\sigma_{\varepsilon_\infty}$ is in very good agreement with the standard deviations obtained from numerical simulations as shown in figure 5.2, where we plot $\sigma_{\varepsilon_\infty}$ as a function of k_0 when $\eta_0 = 5 \times 10^{-4}$ and $\eta_0 = 10^{-3}$. It is worth noting that as long as (3.3) holds, the leading-order behavior of σ_ε is nearly linear in $\eta_0 k_0$.

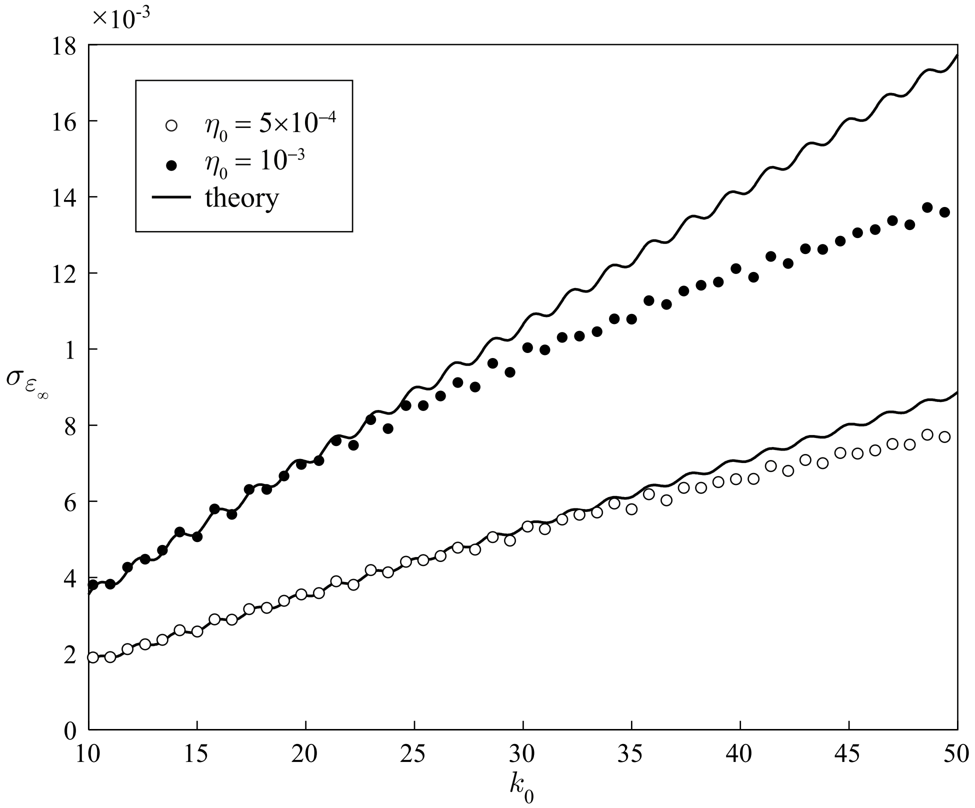

FIGURE 9. Variation of $\langle\theta_{\text{app}}\rangle$ as a function of k_0 for different $\eta_0 = 5 \times 10^{-4}$, 10^{-3}, 5×10^{-3} and 10^{-2}. Wetting inhibition increases as the characteristic substrate parameters, η_0 and k_0 increase. The means were computed for discrete values of k_0, but the lines were joined for the sake of clarity.

6. Nonlinear effects

The formalism developed in the previous sections primarily deals with "weakly" rough substrates so that linearization can be carried out. For substrates that lie beyond the regime of validity of our linearization scheme imposed by the condition (3.3), no analytical prediction can be made and we have to resort to a purely numerical investigation using the full dynamic equations (2.5).

As noted earlier, undulations in the substrate topography are expected to impede the motion of the droplet. As these undulations become more frequent (i.e. k_0 increases), they should naturally inhibit spreading to a greater extent. This holds provided that air is not trapped between the substrate and the droplet. Figure 9 shows plots of $\langle\theta_{\text{app}}\rangle/\theta_{\text{flat}}$ as a function of k_0 for different η_0. There is a monotonic increase in the apparent contact angle, which is indicative of wetting inhibition. This substrate-induced hysteresis effect increases with k_0 and η_0 and for large k_0, there is a linear increase in the apparent contact angle. Unfortunately our present theory cannot rationalize this behavior analytically, which then precludes the rigorous derivation of a Wenzel-like formula to describe substrate-induced hysteresis as a function of surface roughness for two-dimensional substrates.

In figure 10 we plot the probability density function of θ_{app} at different times for a substrate family with $\eta_0 = 10^{-3}$ and $k_0 = 100$, by solving numerically (2.5) for 10^4 members of this substrate family. At early times, the probability densities are highly concentrated about the mean, which roughly corresponds to the apparent contact angle when $\eta(x) = 0$. At later times, when the effects of the topography are more strongly felt, θ_{app} becomes more broadly and less symmetrically distributed about the mean. In the long-time limit, shown at the inset of figure 10, we observe that there can exist substrate realizations that enhance wetting, even though the average behavior inhibits wetting. By calculating the area of the shaded region, we can infer that there is a finite probability (about 10%) for which wetting enhancement occurs, i.e. $\theta_{\text{app}} \leqslant 1$. Consequently wetting inhibition is meant to be taken in an "averaged sense", since not all realizations may exhibit such behavior.

Wetting inhibition occurs not only for advancing fronts, but also for receding ones. To illustrate this, we performed numerical experiments over 10^4 substrate realizations by solving numerically (2.5) for droplet fronts that both initially advance, $a(0) = -b(0) = 1$ and recede, $a(0) = -b(0) = 2$. As noted by Savva & Kalliadasis (2009), a droplet front may not exhibit a single behavior (i.e. either advancing or receding) for all times, but can both advance and recede during its motion, especially when the droplet is close to its equilibrium. The results of our computations are shown in figure 11, where we plot $\theta_{\rm app}$ as a function of the rate of change of the droplet radius, $(\dot{a} - \dot{b})/2$. Due to the substrate-induced hysteresis effect, it is generally observed that the apparent contact angle at equilibrium for advancing fronts, $\theta_{\rm a}$, is different from the apparent contact angle at equilibrium for receding ones, $\theta_{\rm r}$. In this particular case we have that on average $\theta_{\rm a} - \theta_{\rm r} \approx 0.08$. As we show in figure 11, an ensemble average at each time step yields a smooth, one-to-one, curve (solid line) compared to a more oscillatory curve about the mean for a particular substrate realization (dashed line). During such oscillations, the moving fronts usually exhibit stick-slip behavior.

Stick-slip dynamics is difficult to characterize because there can exist a wide variability on how and when stick-slip events occur. Using the same computations as those of figure 10 we depict in figure 12 some representative cases where stick-slip occurs. Low-amplitude heterogeneities do not significantly affect the moving fronts at the onset of spreading, since in all cases presented in the figure, the evolution is nearly indistinguishable from the flat-substrate case for small t. Different stick-slip behaviors occur, however, as the droplet approaches equilibrium and its speed is low enough so that the topographical variations become important. For example, in figure 12(*a*) the left contact point (lcp) gets pinned whereas the right one (rcp) continues to move in a series of weak pinning, de-pinning events. In figure 12(*b*), both fronts appear to be stuck for some time before the rcp depins. Stick-slip events commonly occur for one of the contact points. However depinning can happen for both the rcp and lcp, as figure 12(*c*) indicates. It also possible for multiple stick-slip events to occur for a single front (see figure 12*d*). Figure 12(*e*) shows that stick-slip can occur even at long times and figure 12(*f*) that consecutive depinning events can happen close to each other. Figures 12(*g*–*h*) show the corresponding spreading rates for

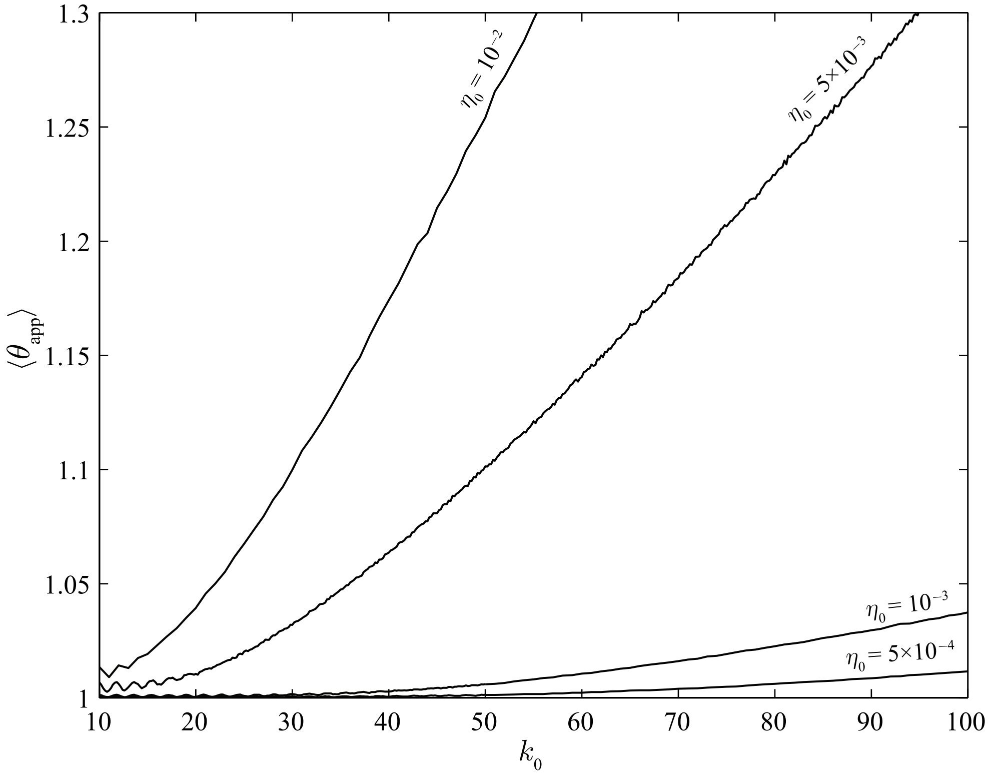

FIGURE 10. Evolution of the probability density of θ_{app} when $\eta_0 = 10^{-3}$ and $k_0 = 100$. The densities $p_0, p_1, \ldots, p_{10}$ correspond to times $t = 0$, 0.2, 0.4, 0.6, 1, 1.5, 3, 5, 10, 50 and 500, respectively. At $t = 0$, we assume a deterministic apparent contact angle $\theta_{\text{app}} = 3$. The discrete points of each probability density have been joined for clarity and the dashed curves show the location of the mean. Inset: the probability density of θ_{app} in the long-time limit. The shaded-region indicates that a substrate realization may enhance wetting with finite probability.

figures 12(*e*–*f*). Despite the remarkable similarity in the evolution of the spreading rates, the relatively minor differences lead to a markedly different evolution for the two moving fronts.

7. Generalization to arbitrary substrate representations

As we demonstrated in §6 of Part 1, the leading-order standard deviation of ε is qualitatively independent of the parametrization we use with respect to k_0 and η_0, apart from

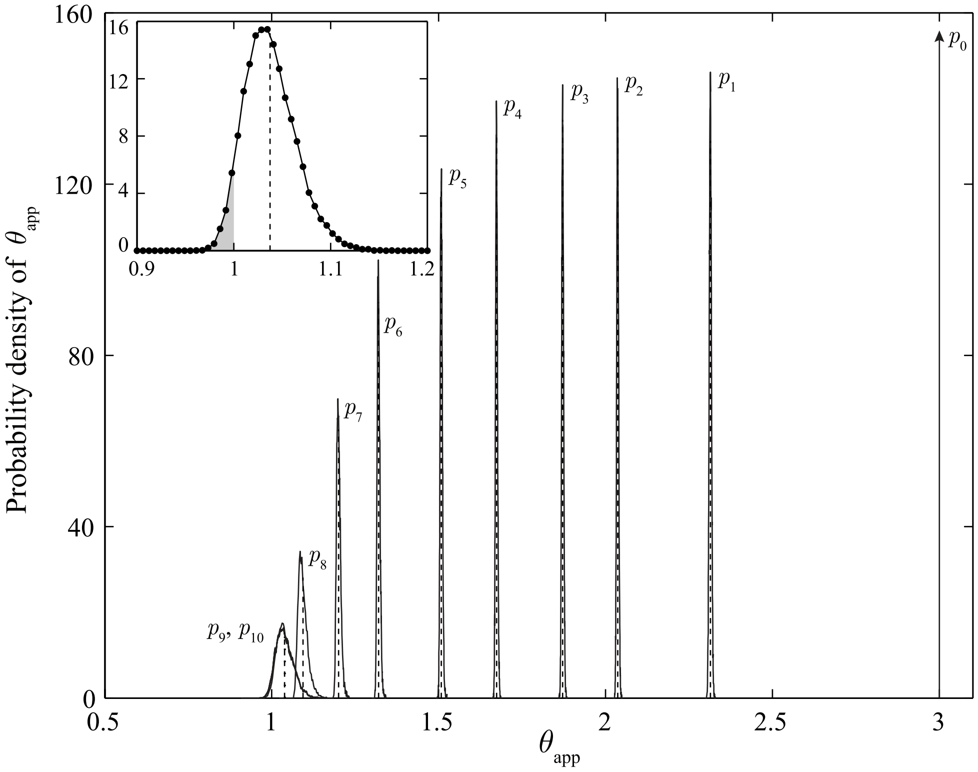

FIGURE 11. Apparent contact angle as a function of the rate of change of the droplet radius, illustrating substrate-induced contact angle hysteresis. For each numerical experiment, the droplet lies initially either at $a(0) = -b(0) = 1$ (advancing) or at $a(0) = -b(0) = 2$ (receding). The solid line corresponds to the curve obtained for an ensemble average taken for fixed t over 10^4 different substrates. The dashed line shows a sample evolution curve for a particular realization.

a numerical prefactor that depends on the specifics of the spectral density function of the substrate. As we shall see in what follows however, there can exist lengthscales, that naturally arise from a substrate family and are able to encompass all the information contained in this prefactor. Contrary to Part 1, we also have additional information concerning the stability of droplet equilibria that we will also incorporate in our analysis. This is accomplished by appropriately casting our problem as one that bears some similarities with a classical problem in probability theory, that of determining the statistics of the maxima of a stationary random function (Rice 1939).

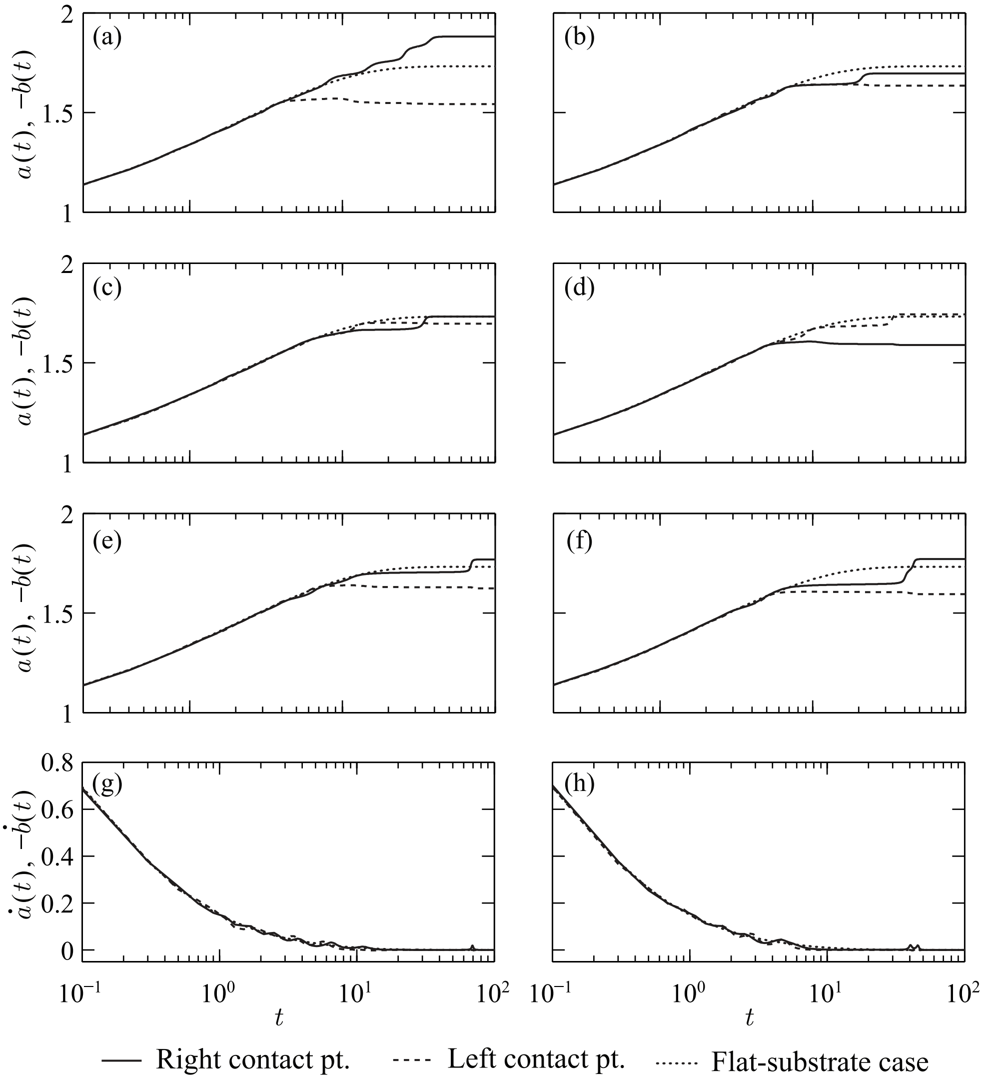

FIGURE 12. Demonstration of pinning-depinning dynamics using examples from numerical experiments using random realizations of (2.1). Plots (a–f) show the evolution curves of $a(t)$ (solid lines) and $-b(t)$ (dashed lines), illustrating different pinning de-pinning scenarios. At the onset all droplets are oblivious to the substrate variations and the evolution curves nearly follow the flat-substrate evolution curve (dotted line). Topography effects become important when the droplet spreads sufficiently slowly. Plots (g) and (h) show the spreading rates for plots (e) and (f) respectively. The final location of the droplet is markedly different regardless of the fact that the spreading rates resemble each other.

Since wetting is sufficiently characterized by the statistics of ε at a stable equilibrium, we only focus on ε, no longer requiring for ℓ to be the closest equilibrium to $\ell = 0$. Thus, for a general substrate with spectral density $S(k)$, given by

$$\eta(x) = \sum_{m=1}^{+\infty} (\alpha_m \sin k_m\ell + \beta_m \cos k_m\ell)\sqrt{S(k_m)\Delta k},$$

where $k_m - k_{m-1} = \Delta k$ and $k_1 = 0$, we need to determine the statistics of

$$\varepsilon = \frac{1}{2}\sum_{m=1}^{+\infty} (\alpha_m \sin k_m\ell + \beta_m \cos k_m\ell)\, F\left(k_m\sqrt{3}\right)\sqrt{S\left(k_m\right)\Delta k}, \tag{7.1}$$

which is the same as (6.3a) of Part 1. Since ℓ is not arbitrary we have the additional constraints:

$$\sum_{m=1}^{+\infty} (\alpha_m \cos k_m\ell - \beta_m \sin k_m\ell)\, G\left(k_m\sqrt{3}\right)\sqrt{S\left(k_m\right)\Delta k} = 0, \tag{7.2a}$$

$$\sum_{m=1}^{+\infty} k_m\left(\alpha_m \sin k_m\ell + \beta_m \cos k_m\ell\right) G\left(k_m\sqrt{3}\right)\sqrt{S\left(k_m\right)\Delta k} > 0. \tag{7.2b}$$

The first equation above is the same as (6.3b) of Part 1 and the second one is the generalization of the stability criterion, given by (4.3). We readily see that the ℓ's that satisfy (7.2) give the locations of the maxima of:

$$Q\left(\ell\right) = \sum_{m=1}^{+\infty} (\alpha_m \sin k_m\ell + \beta_m \cos k_m\ell)\, k_m^{-1} G\left(k_m\sqrt{3}\right)\sqrt{S\left(k_m\right)\Delta k}. \tag{7.3}$$

Rice (1939) investigated the distribution of maxima for stationary random functions such as the one in (7.3). He obtained an analytical expression for their probability density function given by

$$-n_Q^{-1}\int_{-\infty}^{0} \zeta\tilde{p}\left(Q, 0, \zeta\right)\,\mathrm{d}\zeta, \tag{7.4}$$

where n_Q is the number of maxima of Q per unit length and $\tilde{p}\left(Q, Q', Q''\right)$ is the joint probability density function of the Gaussian random variables Q, Q' and Q'', where the primes denote differentiation of a function with respect to its argument (in this case ℓ).

Here we are interesting in the statistics of the additional equation (7.1) not present in Rice's original analysis.

Since ε is correlated with Q and its derivatives, we consider their joint probability density function, $p\left(Q, Q', Q'', \varepsilon\right)$, given in terms of $\mathbf{x} = \left[Q, Q', Q'', \varepsilon\right]^T$ and the square matrix composed of the second moments of the $\mathbf{x}$'s for fixed ℓ, $\mathbf{M}$,

$$p\left(Q, Q', Q'', \varepsilon\right) = \frac{1}{4\pi^2\sqrt{\|\mathbf{M}\|}} \exp\left(-\frac{1}{2}\mathbf{x}^T\mathbf{M}^{-1}\mathbf{x}\right),$$

where $\|\mathbf{M}\|$ and $\mathbf{M}^{-1}$ represent the determinant and inverse of $\mathbf{M}$, respectively (Cramér 1962). The entries of $\mathbf{M}$ are

$$\mathbf{M} = \begin{bmatrix} \left\langle Q^2\right\rangle_\ell & 0 & \left\langle QQ''\right\rangle_\ell & \left\langle Q\varepsilon\right\rangle_\ell \\ 0 & \left\langle Q'^2\right\rangle_\ell & 0 & 0 \\ \left\langle QQ''\right\rangle_\ell & 0 & \left\langle Q''^2\right\rangle_\ell & \left\langle Q''\varepsilon\right\rangle_\ell \\ \left\langle Q\varepsilon\right\rangle_\ell & 0 & \left\langle Q''\varepsilon\right\rangle_\ell & \left\langle \varepsilon^2\right\rangle_\ell \end{bmatrix},$$

where $\langle\cdot\rangle_\ell$ denotes an ensemble average for fixed ℓ. In this general formulation, the probability density function of ε is given by:

$$P\left(\varepsilon\right) = -n_Q^{-1}\int_{-\infty}^{+\infty}\int_{-\infty}^{0} \zeta p\left(\xi, 0, \zeta, \varepsilon\right)\,\mathrm{d}\zeta\,\mathrm{d}\xi,$$

which comes from (7.4) and an integration over all attainable values for Q. In terms of the entries of M, n is given by (Rice 1945):

$$n_Q = \frac{1}{2\pi}\sqrt{\frac{M_{3,3}}{M_{2,2}}}.$$

We can determine $P\left(\varepsilon\right)$ analytically, but here we are primarily interested in determining $\langle\varepsilon\rangle$ and $\left\langle\varepsilon^2\right\rangle$, since we have already found that ε is nearly a normal variable. From the probability density function of ε, we can extract, after some rather lengthy algebra, analytical expressions for the first two moments of ε, given as:

$$\langle\varepsilon\rangle = -M_{3,4}\sqrt{\frac{\pi}{2M_{3,3}}},$$
$$\left\langle\varepsilon^2\right\rangle = M_{4,4} + \frac{M_{3,4}^2}{M_{3,3}}.$$

The expressions above provide information about the statistics of ε in the most general form. However, as we ideally want to investigate the "roughest" substrates permitted by the perturbation condition (3.3), we will proceed by obtaining the leading-order expressions with respect to some large scale, taken to be an upper cutoff wavelength k_c, for which $S\left(k\right) = 0$ for $k > k_c$. The second moments, $M_{3,3}$, $M_{3,4}$ and $M_{4,4}$ are expressed in terms of the autocovariance function of $\eta\left(x\right)$ and its derivatives, given by:

$$\psi_\tau = \left\langle\eta\left(x\right)\eta\left(x+\tau\right)\right\rangle = \int_0^{+\infty} S\left(k\right)\cos k\tau\,\mathrm{d}k.$$

In particular, for "rough" substrates, the most important contributions come from the first two terms from each of the following:

$$M_{4,4} = \left\langle\varepsilon^2\right\rangle_\ell \sim -\frac{3}{8}\psi_0'' - \frac{3}{8}\int_0^{k_c} k^2 S\left(k\right)\cos 2k\sqrt{3}\,\mathrm{d}k,$$
$$M_{3,3} = \left\langle Q''^2\right\rangle_\ell \sim \frac{3}{2}\psi_0'''' + \frac{3}{2}\int_0^{k_c} k^4 S\left(k\right)\cos 2k\sqrt{3}\,\mathrm{d}k,$$
$$M_{3,4} = \left\langle\varepsilon Q''\right\rangle_\ell \sim -\frac{\sqrt{3}}{2}\psi_0'' + \frac{3}{4}\int_0^{k_c} k^3 S\left(k\right)\sin 2k\sqrt{3}\,\mathrm{d}k.$$

Contributions due to a lower cutoff wavenumber, say k_l, are neglected on the basis of the assumption that $k_c \gg k_l$. Furthermore, with the most generality, the spectral density is taken to have $m_c \in \mathbb{N}_0 = \{0,\ 1,\ 2,\ldots\}$ vanishing derivatives at $k = k_c$ so that near k_c it behaves like

$$S\left(k\right) \sim \frac{S_c}{m_c!}\left(k-k_c\right)^{m_c} + O\left(\left(k-k_c\right)^{m_c+1}\right),$$

where S_c is some constant. Hence, we have that, for $m_c = 2n$, $n \in \mathbb{N}_0$,

$$\begin{aligned}
M_{4,4} &\sim -\frac{3}{8}\psi_0'' - \frac{3}{8}\left(-\frac{1}{12}\right)^n k_c^3 S_c \operatorname{sinc} 2k_c\sqrt{3},\\
M_{3,3} &\sim \frac{3}{2}\psi_0'''' + \frac{3}{2}\left(-\frac{1}{12}\right)^n k_c^5 S_c \operatorname{sinc} 2k_c\sqrt{3},\\
M_{3,4} &\sim -\frac{\sqrt{3}}{2}\psi_0'' + \frac{3\sqrt{3}}{2}\left(-\frac{1}{12}\right)^{n+1} k_c^3 S_c \cos 2k_c\sqrt{3},
\end{aligned}$$

and for $m_c = 2n+1$ that:

$$\begin{aligned}
M_{4,4} &\sim -\frac{3}{8}\psi_0'' - \frac{3}{8}\left(-\frac{1}{12}\right)^{n+2} k_c^2 S_c \cos 2k_c\sqrt{3},\\
M_{3,3} &\sim \frac{3}{2}\psi_0'''' + \frac{3}{2}\left(-\frac{1}{12}\right)^{n+2} k_c^4 S_c \cos 2k_c\sqrt{3},\\
M_{3,4} &\sim -\frac{\sqrt{3}}{2}\psi_0'' - \frac{3\sqrt{3}}{2}\left(-\frac{1}{12}\right)^{n+1} k_c^4 S_c \operatorname{sinc} 2k_c\sqrt{3}.
\end{aligned}$$

For the variance of ε, we see that $M_{4,4} \gg M_{3,4}/M_{3,3}$ and hence $\left\langle \varepsilon^2 \right\rangle \sim M_{4,4}$. This proves a result we have previously obtained in Part 1 using less rigorous arguments. Hence

$$\left\langle \varepsilon^2 \right\rangle \sim \begin{cases} -\frac{3}{8}\psi_0'' - \frac{3}{8}\left(-\frac{1}{12}\right)^n k_c^3 S_c \operatorname{sinc} 2k_c\sqrt{3}, & m_c = 2n \\ -\frac{3}{8}\psi_0'' - \frac{3}{8}\left(-\frac{1}{12}\right)^{n+2} k_c^2 S_c \cos 2k_c\sqrt{3}, & m_c = 2n+1, \end{cases}$$

where the contributions due to ψ_0'' are the highest. For the mean of ε, we have that

$$\langle \varepsilon \rangle \sim \begin{cases} \sqrt{\frac{\pi}{4\psi_0''''}}\left[\psi_0'' - 3\left(-\frac{1}{12}\right)^{n+1} k_c^3 S_c \cos 2k_c\sqrt{3}\right], & m_c = 2n \\ \sqrt{\frac{\pi}{4\psi_0''''}}\left[\psi_0'' + 3\left(-\frac{1}{12}\right)^{n+1} k_c^4 S_c \operatorname{sinc} 2k_c\sqrt{3}\right], & m_c = 2n+1, \end{cases}$$

where both terms are now of the same order. Here $\langle \varepsilon \rangle$ and $\left\langle \varepsilon^2 \right\rangle$ depend on integrals of the spectral density function, ψ_0'' and ψ_0''''. Interestingly, knowledge of the number of zero crossings of the substrate per unit length, n_{zeros}, the number of maxima per unit length, $n_{\max}$, and their mean, $\bar{\eta}_{\max}$, suffice to determine ψ_0'' and ψ_0''''. Consequently, it is not necessary to know $S(k)$ everywhere to compute these integrals, since all the required information is contained in these three lengthscales. Hence, we have that (Rice 1945):

$$n_{\mathrm{zeros}} = \frac{1}{\pi}\sqrt{-\frac{\psi_0''}{\psi_0}}, \qquad n_{\max} = \frac{1}{2\pi}\sqrt{-\frac{\psi_0''''}{\psi_0''}} \quad \text{and} \quad \bar{\eta}_{\max} = \frac{\sqrt{10\pi\psi_0}}{6}. \tag{7.5}$$

Thus, by eliminating ψ_0 from the above expressions and solving for ψ_0'' and ψ_0'''' yields:

$$\psi_0'' = -\frac{18}{5}\pi n_{\text{zeros}}^2 \bar{\eta}_{\text{max}}^2$$
$$\psi_0'''' = \frac{72}{5}\pi^3 n_{\text{max}}^2 n_{\text{zeros}}^2 \bar{\eta}_{\text{max}}^2$$

and therefore:

$$\left\langle \varepsilon^2 \right\rangle \sim \begin{cases} \dfrac{27}{20}\pi n_{\text{zeros}}^2 \bar{\eta}_{\text{max}}^2 - \dfrac{3}{8}\left(-\dfrac{1}{12}\right)^n k_c^3 S_c \operatorname{sinc} 2k_c\sqrt{3}, & m = 2n \\ \dfrac{27}{20}\pi n_{\text{zeros}}^2 \bar{\eta}_{\text{max}}^2 - \dfrac{3}{8}\left(-\dfrac{1}{12}\right)^{n+2} k_c^2 S_c \cos 2k_c\sqrt{3}, & m = 2n+1, \end{cases} \tag{7.6}$$

$$\left\langle \varepsilon \right\rangle \sim \begin{cases} -\dfrac{3}{10}\sqrt{\dfrac{5}{2}}\bar{\eta}_{\text{max}}\dfrac{n_{\text{zeros}}}{n_{\text{max}}}\left[1 - \dfrac{5k_c^3 S_c \cos 2k_c\sqrt{3}}{72\pi n_{\text{zeros}}^2 \bar{\eta}_{\text{max}}^2 (-12)^n}\right], & m = 2n \\ -\dfrac{3}{10}\sqrt{\dfrac{5}{2}}\bar{\eta}_{\text{max}}\dfrac{n_{\text{zeros}}}{n_{\text{max}}}\left[1 + \dfrac{5k_c^4 S_c \operatorname{sinc} 2k_c\sqrt{3}}{72\pi n_{\text{zeros}}^2 \bar{\eta}_{\text{max}}^2 (-12)^n}\right], & m = 2n+1. \end{cases} \tag{7.7}$$

From these calculations we can also obtain an expression for the roughness coefficient r, defined in (2.3) of Part 1, which is given by

$$r \approx 1 - \frac{1}{2}\psi_0'' = 1 + \frac{9}{5}\pi n_{\text{zeros}}^2 \bar{\eta}_{\text{max}}^2$$

in its more general form.

As we previously mentioned at the beginning of this section, in Part 1 we found that the leading-order expression for $\left\langle \varepsilon^2 \right\rangle$ is qualitatively the same with respect to the characteristic lengthscales η_0 and k_0 regardless of the choice for the spectral density, with the only difference being a prefactor that dependes on additional parameters needed to describe the spectral density function. The present analysis demonstrates that it is possible to get quantitative agreement as well, provided that we use different lengthscales, namely n_{zeros} and $\bar{\eta}_{\text{max}}$, since $\left\langle \varepsilon^2 \right\rangle \sim 27\pi n_{\text{zeros}}^2 \bar{\eta}_{\text{max}}^2/20$. The result is, of course, the same, but the quantitative agreement stems form the fact that n_{zeros} and $\bar{\eta}_{\text{max}}$ already contain information about $S(k)$ (i.e. they depend on the parameters of $S(k)$), whereas η_0 and k_0 do not. The three lengthscales given by (7.5) are easily determined from an experimental substrate profile; determining the next-order term however requires additional information about the behavior of $S(k)$ near k_c. Hence n_{zeros} and $\bar{\eta}_{\max}$ may be regarded, respectively, as the *natural* characteristic wavenumber and amplitude for the substrate family, whereas η_0 and k_0 appear to be more mathematically than physically motivated.

To make the connection with the band-limited white noise used throughout this study for which

$$S\left(k\right)=\begin{cases}\dfrac{\eta_0^2}{k_0}, & 0\leqslant k\leqslant k_c\\ 0, & k>k_c,\end{cases}$$

we have that $m_c=0$, $k_c=k_0$, $S_c=\eta_0^2/k_0$, $n_{\mathrm{zeros}}=k_0\pi^{-1}/\sqrt{3}$, $n_{\max}=k_0\sqrt{3/5}/(2\pi)$ and $\bar{\eta}_{\max}=\eta_0\sqrt{10\pi}/6$. The result is:

$$\begin{aligned}\left\langle \varepsilon^2\right\rangle &\sim \frac{1}{8}\eta_0^2k_0^2\left(1-3\,\mathrm{sinc}\,2k_0\sqrt{3}\right),\\ \left\langle \varepsilon\right\rangle &\sim -\frac{1}{6}\eta_0\sqrt{5\pi}\left(1-\frac{3}{4}\cos 2k_0\sqrt{3}\right).\end{aligned} \tag{7.8}$$

The first term corresponds exactly to the variance of ε obtained earlier, given also that $\left\langle\varepsilon^2\right\rangle \gg \left\langle\varepsilon\right\rangle^2$. The mean of ε, (7.8) differs from the semi-analytical expression (5.4) that was verified by our numerical experiments. The difference between the two expressions is due to the way the problem was posed. To get (5.4), ℓ is treated as a solution to a first passage problem by assuming initial symmetry about the $x-$axis such that $\ell\left(0\right)=0$, whereas (7.8) takes into account all possible stable equilibria.

8. Conclusions

We have presented the first detailed and systematic investigation of the motion of a droplet over randomly and slowly varying shallow substrates in the limit of small contact angles. Building upon the theoretical framework introduced in Part 1 and the results from the recent work of Savva & Kalliadasis (2009) on droplet spreading over deterministic substrates, we obtained a set of differential equations for the time evolution of the droplet shift, ℓ, and the contact line fluctuations, ε, which correspond to the sliding and spreading components of the droplet motion, respectively. These equations cannot be treated with the standard Langevin/Fokker-Planck formalism of stochastic dynamics but they were appropriately simplified for small-substrate amplitudes.

The droplet shift, which is independent of the contact line fluctuations, is governed by a nonlinear differential equation which can only be solved numerically for arbitrary times. However, the early-time and the long-time behavior of the droplet shift can be obtained analytically. In the long-time limit, in particular, we found its variance to scale like $\mathrm{Var}\,[\ell] \sim O(k_0^{-2})$, which is independent of the characteristic amplitude, η_0. On the other hand, the contact line fluctuation is governed by a linear differential equation, and is therefore predicted to be a normally distributed normal variable for all times. Some simplifying assumptions allowed us to deduce the leading-order variance for all times; in the long-time limit in particular, $\mathrm{Var}\,[\varepsilon] \sim O(\eta_0^2 k_0^2)$.

Obtaining the time-evolution of the mean of the contact line fluctuation is a substantially more difficult task due to the dependence of the ε-dynamics on ℓ. However, we were able to deduce the long-time behavior for the mean, which predicts an overall reduction in spreading, thus allowing us to fully assess the influence of substrate roughness on the wetting characteristics. Our theoretical predictions are in excellent agreement with numerical experiments in a regime where $\eta_0 k_0^2 \ll 1$. We also demonstrated a number of intriguing features. In particular, by examining the evolution of ε and ℓ we showed the tendency of the droplet to slide along the substrate without spreading before reaching equilibrium, the presence of a stick-slip behavior that is rather sensitive to the substrate features and the static contact angle and a substrate-induced, hysteresis-like effect. Finally, our analysis was generalized to arbitrary substrate representations. We showed, in particular that the statistics depends on naturally occurring lengthscales such as the mean number of zeros per unit length, the mean number of substrate maxima per unit length and their mean value.

Although the results of the present study are restricted to two dimensions, thus avoiding some of the intricacies of spreading in three dimensions, they nevertheless show that taking into consideration the details of spreading dynamics through a hydrodynamic model obtained from first principles as well as the way by which droplet equilibria are approached in time, is crucial in analyzing the effects of substrate roughness on wetting.

We acknowledge financial support from EPSRC Platform Grant No. EP/E046029.

REFERENCES

Abramowitz, M. & Stegun, I. A. 1964 *Handbook of Mathematical Functions with Formulas, Graphs, and Mathematical Tables*. New York: Dover.

Breiman, L. 1992 *Probability*. SIAM.

Cazabat, A. M. & Cohen-Stuart, M. A. 1986 Dynamics of wetting: effects of surface roughness. *J. Phys. Chem.* **90**, 5845–5849.

Chung, J. Y., Youngblood, J. P. & Stafford, C. M. 2007 Anisotropic wetting on tunable micro-wrinkled surfaces. *Soft Matter* **3**, 1163–1169.

Cox, R. G. 1983 The spreading of a liquid on a rough solid surface. *J. Fluid Mech.* **131**, 1–26.

Cramér, H. 1962 *Random Variables and Probability Distributions*, 2nd edn. Cambridge University Press.

Ehrhard, P. & Davis, S. H. 1991 Non-isothermal spreading of liquid drops on horizontal plates. *J. Fluid Mech.* **229**, 365–388.

Gardiner, C. W. 1985 *Handbook of Stochastic Methods*. Springer.

Gaskell, P. H., Jimack, P. K., Sellier, M. & Thompson, H. M. 2004 Efficient and accurate time adaptive multigrid simulations of droplet spreading. *Int. J. Numer. Meth. Fluids* **45**, 1161–1186.

Gramlich, C. M., Mazouchi, A. & Homsy, G. M. 2004 Time-dependent free surface Stokes flow with a moving contact line. II. Flow over wedges and trenches. *Phys. Fluids* **16**, 1660–1667.

Hocking, L. M. 1983 The spreading of a thin drop by gravity and capillarity. *Q. J. Mech. Appl. Math.* **36**, 55–69.

Huh, C. & Scriven, L. E. 1971 Hydrodynamic model of steady movement of a solid/liquid/fluid contact line. *J. Coll. Interface Sci.* **35** (1), 85–101.

Kalliadasis, S. 2000 Nonlinear instability of a contact line driven by gravity. *J. Fluid Mech.* **413**, 355–378.

Katzav, E., Adda-Bedia, M., Amar, M. B. & Boudaoud, A. 2007 Roughness of moving elastic lines: crack and wetting fronts. *Phys. Rev. E* **76**, 051601.

Moulinet, S., Guthmann, C. & Rolley, E. 2002 Roughness and dynamics of a contact line of a viscous fluid on a disordered substrate. *Eur. Phys. J. E* **8**, 437–443.

Nikolayev, V. S. 2005 Dynamics and depinning of the triple contact line in the presence of periodic surface defects. *J. Phys. Condens. Matter* **17**, 2111–2119.

Rednikov, A. Y., Rossomme, S. & Colinet, P. 2009 Steady microstructure of a contact line for a liquid on a heated surface overlaid with its pure vapor: Parametric study for a classical model. *Multiphase Sci. Technol.* **21**, 213–248.

Rice, S. O. 1939 The distribution of maxima of a random curve. *Am. J. Math.* **61**, 409–416.

Rice, S. O. 1945 The mathematical analysis of random noise. *Bell System Tech. J.* **23, 24**, reprinted in *Noise and Stochastic Processes* (ed. Wax, N.). Dover 1954.

Savva, N. & Kalliadasis, S. 2009 Two-dimensional droplet spreading over topographical substrates. *Phys. Fluids* **21**, 092102.

Schwartz, L. W. 1998 Hysteretic effects in droplet motions on heterogeneous substrates: direct numerical simulation. *Langmuir* **14**, 3440–3453.

Schwartz, L. W. & Eley, R. R. 1998 Simulation of droplet motion on low-energy and heterogeneous surfaces. *J. Colloid Interface Sci.* **202**, 173–188.

Sodtke, C., Ajaev, V. S. & Stephan, P. 2008 Dynamics of volatile liquid droplets on heated surfaces: theory versus experiment. *J. Fluid Mech.* **610**, 343–362.

Tanguy, A. & Vettorel, T. 2004 From weak to strong pinning I: A finite size study. *Eur. Phys. J. B* **38**, 71–82.

Troian, S., Herbolzheimer, S., Safran, S. & Joanny, J. 1989 Fingering instabilities of driven spreading films. *Europhys. Lett.* **10**, 25–39.